October 19, 2016

Henri Menke

Master Thesis

Topological Superconductivity in Artificial Heterostructures

Max Planck Institute for Solid State Research
Heisenbergstraße 1
70569 Stuttgart, Germany

Institute for Condensed Matter Theory
Pfaffenwaldring 57
70550 Stuttgart, Germany

Supervisor
Dr. A. P. Schnyder

Examiner
Prof. Dr. W. Metzner

Opponent
Prof. Dr. M. Daghofer

This work was typeset
using the ConTEXt MKIV document processor
based on the LuaTEX typesetting system.

The body text is typeset in Lucida Bright
designed by Charles Bigelow and Kris Holmes.

Typographical decisions were based on recommendations
given in *The Elements of Typographic Style* by Robert Bringhurst
and *Detailtypografie* by Friedrich Frossman and Ralf de Jong.

Contents

3 | Contents

5 | Introduction

Chapter 1
7 | Motivation

1.1 Topological Quantum Error Correction 7
1.2 The Toric Code 8
1.3 Relation to Topological Superconductivity 10

Chapter 2
13 | Topological Superconductivity

2.1 Kitaev's Majorana Chain 13
2.2 Chiral p-wave Superconductor 25
2.3 Engineering Topological Superconductivity 31

Chapter 3
33 | Magnetic Adatoms

3.1 Shiba States 33
3.2 Spin Texture 35
3.3 Spin–Orbit Coupling in Solid State Physics 36
3.4 Topological Phases in a Shiba Chain 37
3.5 Chiral States in a Shiba Lattice 46

Appendix A
57 | Algorithms

A.1 Chern Number 57

61 | Summary

65 | References

Introduction

Since the successful fabrication of topological insulators in the last decade [1], tremendous progress has been made in understanding and optimizing these non-trivial topological phases of matter. In mathematics, topology is the study of structures which are classified according to their invariance under continuous deformations. These mathematical methods can be applied to the quantum mechanical wave function, revealing that topologically non-trivial states cannot be adiabatically connected to trivial ones.

The best known and also the first reported non-trivial topological state is the quantum Hall state, discovered by v. Klitzing *et al.* [2]. The chiral edge states of the quantum Hall phase give rise to the quantised Hall conductance observed in experiments. Thouless *et al.* [3] showed that this conductance is related to the topological invariant of the system, called the Chern number or the TKNN invariant. A lot of effort has been taken to identify these invariant quantities for other systems and their interplay with symmetries has led to an exhaustive classification for non-interacting systems [4–7].

Topological insulators are gapped in the normal phase and exhibit gapless edge modes in the topological phase while the bulk remains gapped. A gapped spectrum is not exclusive to an insulator. In superconductors the BCS ground state is separated from the quasiparticle excitation spectrum by the superconducting gap [8]. In contrast to topological insulators the gapless surface states are superpositions of particle- and hole-like excitations. This is an analogy to particle and anti-particle pairs which allows a description in terms of Majorana fermions. Kitaev [9] showed that the edge modes in a one-dimensional p-wave superconductor have Majorana character.

Majorana fermions have been proposed as a platform for quantum computation [10]. However, intrinsic topological superconductors are rare in nature. Artificial heterostructures can be designed and fabricated in a lab and various proposals for proximity induced topological superconductivity exist. The most promising approach is to deposit magnetic adatoms on the surface of a conventional s-wave superconductor [11–14]. Magnetic impurities induce low-energy Shiba bound states in the gap which hybridise and form bands in the limit of dense impurities. Depending on the orientation of the classical impurity spins and intrinsic spin–orbit coupling in the superconductor these bands exhibit non-trivial topology [15].

In this thesis we will design an artificial heterostructure between a conventional s-wave superconductor with strong spin–orbit coupling and non-collinear magnets. We evaluate under which conditions Majorana edge states can form and obtain the topological phase diagram. For two-dimensional interfaces we

additionally extract the spontaneous surface current resulting from the chiral edge states. We investigate these properties using both analytical methods as well as numerical tight-binding calculations.

Chapter 1

Motivation

It is a common misconception that a quantum computer is intrinsically faster than its classical counterpart. This assertion holds true only for a very limited set of algorithms. But the implementation of these highly specialised algorithms promises a polynomial or even exponential speed-up.

Many of these specialised algorithms are mere proofs-of-concept accompanied by a few real-world use cases, such as Grover's algorithm [16] for searching entries in an unsorted dictionary or Shor's famous algorithm [17] for the prime factorisation of integers. Alongside this so called *digital* quantum simulation where computational operations are realised with logical quantum gates there exists the concept of *analog* quantum simultion where a quantum system is implemented in terms of another one. For instance, the Hubbard model could be implemented using cold atoms in an optical lattice [18,19].

Quantum computation's most crucial obstacle is *decoherence*. A quantum state is in general entangled with its environment leading to dissipation of the probability amplitude, which can be modelled by means of non-unitary processes. This is captured by either a semigroup approach generated by Lindblad superoperators [20] or a completely non-Hermitian formulation of quantum mechanics [21]. Loss of information results in errors creeping into the computational steps. In contrast to classical error correction we now require some form of *quantum* error correction.

1.1 Topological Quantum Error Correction

Classical information is stored in the form of magnetic charges (hard disk drives) or electric charges (flash memory, such as RAM or solid-state drives). To compensate for the loss of information, due to physical failure of the storage components, known as data rot, one introduces redundancy by *copying* the data somewhere else for a later restore.

For a quantum system this is forbidden by the no-cloning theorem which states that it is in general not possible to make a copy of an unknown quantum state. Thus we cannot simply store recovery information for quantum bits. But errors can be corrected by distributing the information over several qubits. The Shor code for instance distributes the encoded information onto nine qubits and

can correct any single qubit error from their entanglement. A variety of *active* error correction codes has been devised [22], but it would be much easier if the integrity of the storage was *protected* by self-correction since active algorithms have a very low accuracy threshold [23].

1.2 The Toric Code

The Toric Code Model (TCM) was proposed by Kitaev [24]. The system with all the subsequently introduced operations is visualised in figure 1.1. We start from a square lattice with $k \times k$ sites and periodic boundary conditions in both directions. That is to say, the system is embedded in a torus $\mathbb{T}_2$. To each edge connecting two sites we attach a spin $1/2$, such that there are $n = 2k^2$ qubits in total. By concatenating these edges we can form certain structures on the lattice, two of which are of particular importance; the star s and the plaquette p. The two *stabilizer* operators

$$A_s = \prod_{j \in \text{star}(s)} \sigma_j^x \quad \text{and} \quad B_p = \prod_{j \in \text{boundary}(p)} \sigma_j^z \tag{1.1}$$

mutually commute, because a star and a plaquette share either two or no edges. They both possess eigenvalues ± 1. Now we define the *protected subspace* of the full Hilbert space of all qubits.

$$\mathcal{L} = \{|\xi\rangle \in \mathcal{H} \mid A_s |\xi\rangle = |\xi\rangle, B_p |\xi\rangle = |\xi\rangle, \forall s, p\} . \tag{1.2}$$

That is to say, that $\mathcal{L}$ comprises all qubits which are invariant with respect to all star and plaquette operators. Now the question is, what is the dimension of this protected subspace—or in other words—how many protected qubits can we encode in the Toric code?

In a lattice of size $k \times k$ we can identify k^2 different stars and k^2 different plaquettes, i.e. there are at most $2k^2$ operators. However, we observe that these operators have the property

$$\prod_s A_s = 1 \quad \text{and} \quad \prod_p B_p = 1 \tag{1.3}$$

which indicates that there are only $m = 2k^2 - 2$ *independent* operators. Using the general theory of additive quantum codes, Kitaev [24] concludes that $\dim \mathcal{L} = 2^{n-m} = 2^2 = 4$, i.e. the Toric code model encodes *two logical qubits*. This construction is not restricted to a square lattice, but can be extended to any two-dimensional orientable manifold. The ground state is then 4^g-fold degenerate where g is the number of holes in the support of the lattice.

As we have discussed, states in the protected subspace $\mathcal{L}$ are invariant with

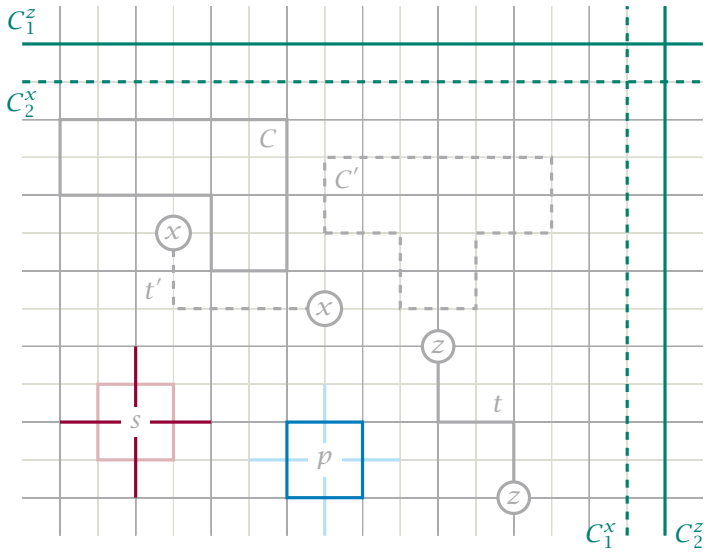

■ *Figure 1.1* Illustration of the basic constructs in the Toric code on a lattice with periodic boundary conditions. The fine lines denote the dual lattice. Star s and plaquette p terms are dual to each other. The loops C and C' as well as the open strings t and t' with excitations on their ends act trivially on the protected subspace. Only the non-trivial loops $C^z_{1,2}$ and $C^x_{1,2}$ wind around the torus.

respect to all star and plaquette operators. An excitation has to violate one of these constraints then. Excitations can only occur in pairs (due to (1.3)) which means there is a path connecting them. The two types of excitations can thus be written like

$$S^z(t) = \prod_{j\in t} \sigma_j^z \quad \text{and} \quad S^x(t') = \prod_{j\in t'} \sigma_j^x \,. \tag{1.4}$$

The excitations are created at the endpoints of the "string" t (t') on the normal (dual) lattice. Closed strings (loops) do not create any excitations, however they do not necessarily act trivially on the Toric code. Non-trivial loops cannot be contracted, which leaves only two possible loops, namely those around the two directions of the torus, which we denote by C_1^z and C_2^z for z-type excitations and C_1^x and C_2^x for x-type excitations. Moving an excitation along these path is equivalent to applying the operator (1.4) for which we define the shorthands with $i = 1, 2$

$$Z_i = S^z(C_i^z) \quad \text{and} \quad X_i = S^x(C_i^x) \,. \tag{1.5}$$

These operators facilitate manipulations on the ground state space. It is no coincidence that the operators are named Z and X. They are the equivalent to σ^z and σ^x for single qubits. We now have the Z operators for readout and X for bit-flip. By moving these excitations around each other (braiding) they pickup a phase, unlike conventional particles. Particles with this property are

called *Abelian anyons*.

The two logical qubits which we have found are robust against *local* perturbations. In fact, any operator comprising phase (σ^z) and bit-flip errors (σ^x), that does not wind around the torus cannot invalidate the ground state. Errors which form closed, contractible loops are not considered errors at all. Open strings have two excitations at the ends which can be detected by measuring all A_s and B_p (syndrome measurement) and corrected by finding the characteristic vector out of the result of this measurement (the syndrome) [24].

Another possibility is to correct errors on a physical level. We introduce the Toric code Hamiltonian as devised in [24]

$$H^{\mathrm{TCM}} = -\sum_s A_s - \sum_p B_p \,. \tag{1.6}$$

Since all A_s and B_p commute one can easily diagonalise this Hamiltonian. The ground state space is equivalent to (1.2) and four-fold degenerate. Excitations always occur in pairs, which means that the ground state is separated by a gap $\Delta \geq 2$ from the excitations spectrum. One expects noise-induced errors to be removed by some sort of relaxation process.

An implementation of the Toric code using ultracold Rydberg atoms has been proposed [25]. The Rydberg blockade is exploited to engineer a quantum simulator. Optical pumping of the control atom into the ground state introduces cooling.

1.3 Relation to Topological Superconductivity

The Toric code model is the prime example of a system with anyonic excitations. However, as noted in the end of the previous section, the Toric code is hard to realise and surrogate models are needed. It was again Kitaev who introduced a system with similar *non-abelian* modes, known as Majorana modes. Majorana fermions are originally a concept of high-energy physics and were hypothesised by Ettore Majorana in 1937. Fermions of this type are their own antiparticles and neutrinos are believed to possibly belong to this class.

Majorana modes arise at the edges of one- or two-dimensional topologically non-trivial superconductors. In one dimension such a model was first proposed by Kitaev [9]. It is so important for the understanding of topological superconductivity that we will devote almost the entire next chapter to its properties and phenomena.

Summary of Chapter 1

Quantum computers promise tremendous speed-ups over their classical counterparts for certain tasks. However, besides scalability the correction of errors is a main show-stopper for the implementation of quantum computers today. One can probably leverage this shortcoming with the help of topologically protected quantum components. The Toric code is the prime example of such a system, however, the actual implementation is still lacking. Topological superconductors can be used to physically realise topologically protected quantum computers. Thus they are hot candidates for building blocks in a topological quantum computer.

Chapter 2

Topological Superconductivity

This chapter will outline some basics about topological superconductivity. Starting with Kitaev's Majorana chain we will show how Majorana fermions can arise in superconductors and sketch how they can be used to achieve error correction. Following this, we have a short glimpse at the chiral p-wave superconductor because it provides a simple showcase for the algorithms needed later.

2.1 Kitaev's Majorana Chain

Majorana fermions arise at the edges of a one-dimensional superconducting quantum wire. They have interesting properties that make them good candidates for a robust quantum storage.

2.1.1 The Toy Model

The Majorana chain was introduced by Kitaev [9] to describe a simple but unrealistic model which exhibits Majorana fermions. Consider a chain of spinless fermions with N sites and p-wave superconductivity. It is described by the following Hamiltonian

$$H = \sum_n (t f_n^\dagger f_{n+1} + \Delta f_n f_{n+1} + \text{H.c.}) - \mu \sum_n \left(f_n^\dagger f_n - \frac{1}{2} \right), \tag{2.1}$$

where f_n are the fermionic annihilation operators and t is the hopping amplitude, Δ the superconducting gap, and μ the chemical potential. If the order parameter of superconductivity was complex as in $\Delta = |\Delta| e^{i\theta}$ one could apply the simple gauge transformation

$$f_n \to f_n = e^{-i\theta/2} \hat{f}_n \quad \text{and} \quad f_n^\dagger \to f_n^\dagger = e^{i\theta/2} \hat{f}_n^\dagger \tag{2.2}$$

to make it real. Henceforth we will assume Δ to be real.

To proceed we introduce self-adjoint creation and annihilation operators

$$\gamma_{2n-1} = f_n + f_n^\dagger \quad \text{and} \quad \gamma_{2n} = -i(f_n - f_n^\dagger) \tag{2.3}$$

which we will from now on call *Majorana operators*. They obey commutation relations defined by the Clifford algebra.

$$\{\gamma_n, \gamma_{m'}\} = 2\delta_{n,m} \quad \text{where} \quad \gamma_n^\dagger = \gamma_n \,. \tag{2.4}$$

Now we transform (2.1) using the definitions of (2.3) and obtain

$$H = \frac{i}{2}\sum_n \left[(\Delta + t)\gamma_{2n-1}\gamma_{2n+2} + (\Delta - t)\gamma_{2n}\gamma_{2n+1}\right] - \mu\frac{i}{2}\sum_n \gamma_{2n-1}\gamma_{2n} \,. \tag{2.5}$$

For open boundary conditions there is a first and a last site, which we are going to refer to as *left mode* $\gamma_1 = \gamma_L$ and *right mode* $\gamma_{2N} = \gamma_R$. Let us now examine two special cases.

The Trivial Case

Let $t = \Delta = 0$, then we find

$$H = -\mu\frac{i}{2}\sum_n \gamma_{2n-1}\gamma_{2n} = -\mu\sum_n \left(f_n^\dagger f_n - \frac{1}{2}\right) . \tag{2.6}$$

Here Majorana operators from the *same physical site* n are paired together to form regular fermions which are perfectly localised.

The Topological Case

Let $\Delta = -t$ and $\mu = 0$. Here things become more peculiar

$$H = -it\sum_n \gamma_{2n}\gamma_{2n+1} \,. \tag{2.7}$$

Now the Majorana operators from two different sites are paired together, leaving the two outermost Majoranas γ_L and γ_R *unpaired*. Note that this is indeed a valid situation, because from a purely algebraic point of view it is irrelevant which two Majoranas are paired to satisfy the inverse transformation of (2.3). Based on this observation we introduce new fermionic modes

$$\alpha_n = \frac{1}{2}(\gamma_{2n} + i\gamma_{2n+1}) \quad \text{and} \quad \alpha_n^\dagger = \frac{1}{2}(\gamma_{2n} - i\gamma_{2n+1}) \,. \tag{2.8}$$

Note that the two unpaired Majoranas γ_L and γ_R do not enter. Thus the Hamiltonian without the edge modes reads

$$H = -2t\sum_n \left(\alpha_n^\dagger \alpha_n - \frac{1}{2}\right) . \tag{2.9}$$

This is formally equivalent to (2.6) but without the two unpaired Majoranas

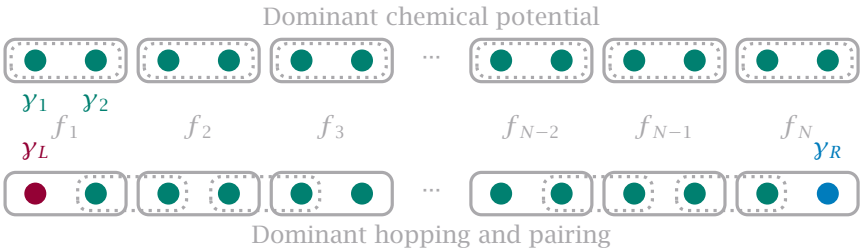

■ *Figure 2.1* The two possible configurations for pairing up the Majorana fermions. Solid boxes are physical sites f_n, dots are Majorana fermions γ_n. *Above* is the trivial case where Majoranas are paired up on the same physical site as indicated by the dashed boxes. *Below* is the topological case where Majoranas are paired up from different physical sites, leaving the two Majoranas γ_L and γ_R at the ends unpaired.

at the edges. Therefore we conclude, that both cases exhibit the same *bulk* properties. Indeed, the two cases (2.6) and (2.7) are related by a transformation $\gamma_m \to \gamma_{m+1}$. However, this transformation is not unitary and thus the phases are not equivalent.

As already noted, in the definition of the α_n operators the two edge modes do not enter. We can pair up the two edge modes to form an additional operator

$$\alpha_N = \frac{1}{2}(\gamma_{2N} + i\gamma_1) = \frac{1}{2}(\gamma_R + i\gamma_L)\,. \tag{2.10}$$

Here we wrapped around after $2N$ and for periodic boundary conditions we would indeed recover a localised fermionic mode. When we write the edge Hamiltonian (2.10) in terms of fermionic operators f_n we find non-local superpositions of the first and the last site which allows us to detect the Majorana fermion in a local density of states measurement at the endpoints of the wire.

2.1.2 Numerical Treatment

For open boundary conditions the Hamiltonian (2.1) can in general not be diagonalised analytically. Nevertheless we can just write it as a matrix which can then be readily diagonalised by a computer. To this end we rewrite (2.1) in a more convenient form using $\psi_n = (f_n, f_n^\dagger)^\top$

$$H = \sum_n \psi_n^\dagger \underbrace{\begin{bmatrix} t & \Delta \\ -\Delta & -t \end{bmatrix}}_{\mathcal{T}} \psi_{n+1} + \sum_n \psi_n^\dagger \underbrace{\begin{bmatrix} -\mu & \\ & \mu \end{bmatrix}}_{\mathcal{M}} \psi_n - \frac{\mu N}{2}\,. \tag{2.11}$$

Because it does not make any difference we neglect the constant energy offset of $-\mu N/2$ and obtain using $\Psi = (\psi_1, \ldots, \psi_N)^\top$

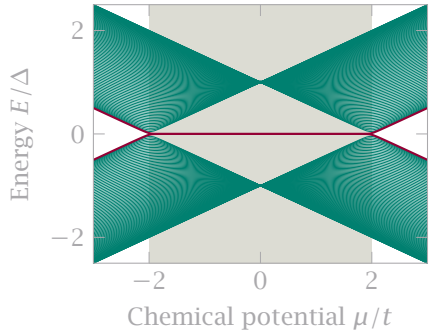

■ *Figure 2.2* We show the excitation spectrum of a Kitaev chain with 100 sites. The green lines correspond the the bulk modes, whereas the red lines form the edge modes in the topological regime. Parameters are $t = 1$, $\Delta = 1$.

$$H = \Psi^\dagger \begin{bmatrix} \mathcal{M} & \mathcal{T} & & \\ \mathcal{T}^\dagger & \mathcal{M} & \mathcal{T} & \\ & \mathcal{T}^\dagger & \ddots & \ddots \\ & & \ddots & \ddots \end{bmatrix} \Psi \,. \tag{2.12}$$

Excitation Spectrum

From the diagonalisation of the matrix (2.12) we can extract the eigenenergies of the chain for any set of parameters. As we will discuss later, the parameters μ and t drive the topological phase transition. Hence we diagonalise the Hamiltonian with open boundary conditions for many values of μ at fixed t and plot all the energy eigenvalues as a function of μ/t.

The resulting excitation spectrum is shown in figure 2.2. We see that the bulk gap closes at $\mu = \pm 2t$. In the topological regime, highlighted by the grey background, a state localised at zero energy splits off from the bulk spectrum. Below we will see that this state is localised at the edges of the wire.

Local density of States

We are interested in the localisation of the Majorana modes. Therefore we compute the local density of states (LDOS) which is given by

$$\rho(x, E) = \sum_i \left[|u_i(x)|^2 \delta(E - E_i) + |v_i(x)|^2 \delta(E + E_i) \right] , \tag{2.13}$$

with u_i and v_i being the coefficients of the particle and hole components of the computed eigenvectors with energy eigenvalue E_i. On a computer the evaluation of the above expression is done on a discrete range of E. As we cannot make the spacing between sampling points arbitrarily small for obvious reasons, we have to approximate the δ distribution, which we do by using a Lorentzian of

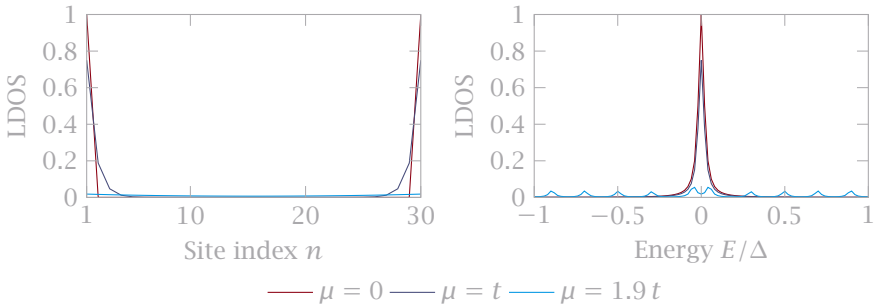

■ *Figure 2.3* Local density of states for different values of the chemical potential. The line broadening was chosen as $\eta = 2 \cdot 10^{-2}$. On the *left-hand side* we show the local density of states in position space at zero energy. On the *right-hand side* we show the local density of states at the first site of the chain, i.e. the left edge in the right picture. With increasing μ the localisation decreases. Parameters are $t = 1, \Delta = 1$.

finite width η

$$\delta(x) = \lim_{\eta \to 0} \mathcal{L}_\eta(x) = -\lim_{\eta \to 0} \operatorname{Im} \frac{\eta}{x + i\eta} \,. \tag{2.14}$$

In figure 2.3 we show the local density of states in position space and in energy space for three different values of the chemical potential μ. At the ideal point ($\mu = 0$) the ground state is perfectly localised at the edges of the wire. For large μ (e.g. $\mu = t$) the edge state protrudes into the bulk (exponential localisation) and in the vicinity of the gap closing $\mu = 1.9\,t$ (the values where the gap closing occurs depends on the system size) the state has entered the bulk spectrum. In the limit of an infinite chain the gap closing shifts to the exact gap closing at $\mu = 2t$. The gap closing transition manifests itself in the LDOS in terms of the vanishing of the zero bias peak which is also the prime signature observed in the current in tunnelling experiments (STM, interference junctions) [13,26].

▶ Disorder Stability

The Majorana modes do not enter the Hamiltonian (2.9) at the ideal point $\mu = 0$. However, to not violate the charge parity we have to pair them up which results in a highly delocalised fermionic mode where one half is located at one end of the wire and the other half at the other end. This non-local character should make the modes very robust against random disorder.

To study this we introduce the site dependent parameters

$$t_n = t(1 + \delta_t(x_n)) \,, \quad \mu_n = \mu(1 + \delta_\mu(x_n)) \,, \quad \Delta_n = \Delta(1 + \delta_\Delta(x_n)) \,, \tag{2.15}$$

where δ_α is a random variable uniformly distributed in the interval Ω_α with

$\alpha \in \{t, \mu, \Delta\}$. As a result, the spectrum becomes noisy in contrast to figure 2.2 where all the lines are smooth. We are interested in how the edge state is affected because according to the above reasoning it should be unaffected by perturbations if the edges are well separated.

In figure 2.4 we show the lowest positive eigenenergy energy as a function of chemical potential for static random disorder in the hopping and the superconducting gap with $\Omega_t = \Omega_\Delta = [-0.5, 0.5]$. Astonishingly, we find that at the ideal point the zero-energy edge state is completely unaffected by disorder even for very short chains. For $\mu \neq 0$ the edge state is only stable in longer chains, since for non-ideal parameters the edge state is not perfectly localised as we saw in the previous discussion of the LDOS.

2.1.3 Bogoliubov-de-Gennes Transformation

For periodic boundary conditions, the Majorana chain (2.1) can be diagonalised analytically. To this end we apply a Fourier transform to the fermionic operators using

$$f_n = \frac{1}{\sqrt{N}} \sum_k e^{ikx_n} f_k \quad \text{and} \quad f_n^\dagger = \frac{1}{\sqrt{N}} \sum_k e^{-ikx_n} f_k^\dagger \,. \tag{2.16}$$

This transformation is unitary, i.e. the commutation relations of the f_k are the same as of the f_n. The f_k do no longer correspond to particles but to modes associated with their lattice momentum. These modes f_k have all the mathematical structure of single particles, yet they describe collective properties of all physical particles.

Plugging (2.16) into (2.1) yields

$$H = \sum_k [2t \cos(k) f_k^\dagger f_k - \mu f_k^\dagger f_k + \Delta e^{-ik} f_k f_{-k} + \Delta e^{ik} f_{-k}^\dagger f_k^\dagger] \,, \tag{2.17}$$

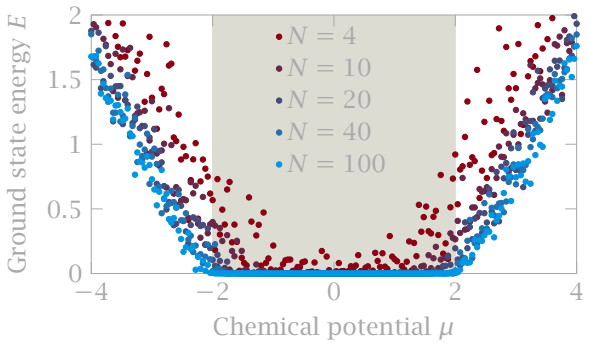

■ *Figure 2.4* We show the ground state energy for different chain lengths as a function of μ with static random disorder in the other parameters where $\Omega_t = \Omega_\Delta = [-0.5, 0.5]$. For sufficient separation of the edges the ground state is unaffected by perturbations completely. Parameters are $t = 1$, $\Delta = 1$.

where we have again disregarded the constant offset of $-\mu N/2$. The terms containing the gap function do not look so nice with the complex phase factors, so we readily remove these by using the substitutions

$$f_k f_{-k} = \frac{1}{2}(f_k f_{-k} - f_{-k} f_k) \quad \text{and} \quad f^\dagger_{-k} f^\dagger_k = \frac{1}{2}(f^\dagger_{-k} f^\dagger_k - f^\dagger_k f^\dagger_{-k}) \,. \tag{2.18}$$

This provides us with the nice form

$$H = \sum_k [(2t\cos(k) - \mu) f^\dagger_k f_k - i\Delta \sin(k) f_k f_{-k} + i\Delta \sin(k) f^\dagger_{-k} f^\dagger_k] \,. \tag{2.19}$$

We proceed to write this Hamiltonian in Nambu grading where $\Psi_k = (f_k, f^\dagger_{-k})^\top$ and find the Bogoliubov-de-Gennes (BdG) Hamiltonian

$$H = \frac{1}{2}\sum_k \Psi^\dagger_k H_k \Psi_k = \frac{1}{2}\sum_k \Psi^\dagger_k \begin{bmatrix} 2t\cos(k) - \mu & 2i\Delta\sin(k) \\ -2i\Delta\sin(k) & -(2t\cos(k) - \mu) \end{bmatrix} \Psi_k \,. \tag{2.20}$$

To extract the spectrum it suffices to diagonalise H_k. We find

$$E(k) = \pm\sqrt{(2t\cos(k) - \mu)^2 + (2\Delta\sin(k))^2} \tag{2.21}$$

Due to the sine function appearing squared there are only two possibilities for the spectrum to be gapless, namely $k = 0$ and $k = \pm\pi$ and we find the following condition for gap closing

$$\pm\sqrt{(\pm 2t - \mu)^2} = 0 \implies 2|t| = |\mu| \,. \tag{2.22}$$

At these two points we expect the quantum phase transition to occur between the trivial phase and the topological phase.

2.1.4 The Topological Phase

Winding Number

Before we start, let us quickly take a look at a general 2×2 matrix of the form

$$M = \boldsymbol{d}\cdot\boldsymbol{\sigma} \quad \text{with} \quad \boldsymbol{d} = \begin{pmatrix} r\sin\theta\cos\phi \\ r\sin\theta\sin\phi \\ r\cos\theta \end{pmatrix} \quad \text{and} \quad \boldsymbol{\sigma} = \begin{pmatrix} \sigma^x \\ \sigma^y \\ \sigma^z \end{pmatrix} . \tag{2.23}$$

The eigenvalues and eigenvectors of such a matrix are given in general by

$$E_\pm = \pm|\boldsymbol{d}| \,, \quad |n+\rangle = \begin{pmatrix} e^{-i\phi}\cos\theta/2 \\ \sin\theta/2 \end{pmatrix} , \quad |n-\rangle = \begin{pmatrix} -e^{-i\phi}\sin\theta/2 \\ \cos\theta/2 \end{pmatrix} . \tag{2.24}$$

The Bogoliubov-de-Gennes Hamiltonian (2.20) can also be written in that form

$$H_k = \boldsymbol{d}(k) \cdot \boldsymbol{\sigma} \quad \text{with} \quad \boldsymbol{d}(k) = \begin{pmatrix} 0 \\ -2\Delta \sin(k) \\ 2t\cos(k) - \mu \end{pmatrix}. \tag{2.25}$$

Clearly, the vector $\boldsymbol{d}(k)$ lives on the cross section through $x = 0$ of the Bloch ball and can be associated a *winding number*. Combining (2.23) with (2.25) we find

$$\begin{aligned} \phi(k) &= \arctan\left(\frac{d_y}{d_x}\right) = \begin{cases} +\pi/2 & -\pi < k < 0 \\ -\pi/2 & 0 < k < \pi \end{cases}, \\ \theta(k) &= \arccos\left(\frac{d_z}{|\boldsymbol{d}|}\right) = \arccos\left(\frac{2t\cos(k) - \mu}{\sqrt{(2t\cos(k) - \mu)^2 + (2\Delta\sin(k))^2}}\right). \end{aligned}$$

The winding number is defined as [27]

$$\Gamma = i \oint_{\mathrm{BZ}} \langle n- | \partial_k | n- \rangle \, \mathrm{d}k = \int_{-\pi}^{\pi} \sin^2(\theta/2) \, \partial_k \phi \, \mathrm{d}k \,. \tag{2.26}$$

The derivative of the piecewise defined function $\phi(k) \sim \Theta(k)$ is a delta distribution. This makes the integration very easy and the result can be readily obtained

$$\Gamma = \frac{\pi}{2} \int_{-\pi}^{\pi} [1 - \cos(\theta)] \delta(k) \, \mathrm{d}k = \frac{\pi}{2}\left(1 - \frac{2t - \mu}{|2t - \mu|}\right) = \begin{cases} 0 & |\mu| > 2|t| \\ \pi/2 & |\mu| = 2|t| \\ \pi & |\mu| < 2|t| \end{cases}. \tag{2.27}$$

This is very interesting. Comparing the above result with the condition for the gap closing in (2.22) we see that the winding number changes from zero to non-zero (or vice versa) when the gap closes. This is exactly the phase transition we were hoping to find and with the winding number Γ we also found the order parameter describing it. Here we also see why topological matter is different from symmetry broken matter. Instead of a *local* function of position the order parameter is a *global* property of the wave function.

The Pfaffian

Kitaev [9] proposed a different but indeed equivalent order parameter based on the properties of the Hamiltonian itself in the quadratic form (2.5). This Hamiltonian can be written as

$$H = \frac{i}{4}\sum_{n,m} A_{nm}\gamma_n\gamma_m \quad \text{with} \quad A_{nm} = -A_{mn}\,. \tag{2.28}$$

The matrix A is called *skew-symmetric* or sometimes also *anti-symmetric*. Matrices of this kind have a property called the *Pfaffian* which Kitaev related to a topological invariant which he termed the Majorana number. It is defined as

$$\mathrm{Pf}[A] = \frac{1}{2^N N!}\sum_{\sigma\in S_{2N}} \mathrm{sgn}(\sigma) A_{\sigma(1),\sigma(2)}\cdots A_{\sigma(2N-1),\sigma(2N)}\,, \tag{2.29}$$

where S_{2N} is the set of $2N$ permutations and $\mathrm{sgn}(\sigma)$ is the parity of the permutation σ. Additionally it holds that $(\mathrm{Pf}[A])^2 = \det[A]$.

Calculating the Pfaffian for open boundary conditions is indeed possible but would involve a numerical evaluation of (2.29). Therefore we will Fourier transform (2.5) for an easier treatment. The prescription for the Fourier transformation of Majorana operators reads

$$\gamma_{2n-1} = \frac{1}{\sqrt{N}}\sum_q e^{-iqn} b_{q,1}\,, \quad \gamma_{2n} = \frac{1}{\sqrt{N}}\sum_q e^{-iqn} b_{q,2}\,. \tag{2.30}$$

Note that $b_q^\dagger = b_{-q}$. After some simple steps we obtain with $b_q = (b_{q,1}, b_{q,2})$

$$H = \frac{i}{4}\sum_q b_q^\dagger \begin{bmatrix} & 2t\cos(q) - \mu + 2i\Delta\sin(q) \\ -2t\cos(q) + \mu - 2i\Delta\sin(q) & \end{bmatrix} b_q\,. \tag{2.31}$$

For a 2×2 matrix the Pfaffian is given by

$$A = \begin{bmatrix} & a \\ -a & \end{bmatrix}, \quad \mathrm{Pf}[A] = a = 2t\cos(q) - \mu + 2i\Delta\sin(q)\,. \tag{2.32}$$

With this result the Majorana number W is given by [4]

$$W = \prod_a \frac{\mathrm{Pf}[A(\Lambda_a)]}{\sqrt{\det[A(\Lambda_a)]}} = \prod_a \mathrm{sgn}(\mathrm{Pf}[A(\Lambda_a)]) = \mathrm{sgn}(\mu^2 - 4t^2) \tag{2.33}$$

where $\Lambda_a = 0, \pi$ are the time-reversal invariant momenta. Apparently, W can only take the values ± 1 and we find the same condition as for the winding number

$$W = \begin{cases} +1 & |\mu| > 2|t| \\ -1 & |\mu| < 2|t| \end{cases}\,. \tag{2.34}$$

For this special case the Majorana number W and the winding number Γ yield the same result for the classification of the topological phase. The winding number is *ab initio* an arbitrary integer, i.e. $\mathbb{Z}$, whereas the Majorana number can only takes two values, i.e. $\mathbb{Z}_2$. Furthermore, the winding number belongs to the symmetry class BDI (real Δ) whereas the Majorana number belong to class D (complex Δ). For class D it was proven rigorously [28] that the winding number and the Majorana number are equivalent. To conclude the discussion we show a topological phase diagram of the Kitaev chain in figure 2.5.

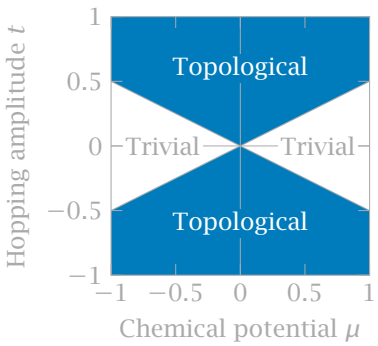

■ *Figure 2.5* Topological phase diagram for the Kitaev chain. We plotted the topological invariant over the two parameters of the model. It is easy to see that at the ideal point ($\mu = 0$) the chain is in the topological phase, regardless of the hopping amplitude.

Unfortunately, this is not the whole story. It turns out very quickly that this classification of topological phases depends on the system under consideration. That is to say, not every Hamiltonian can be classified using the winding number or the Majorana number as shown above. Huge effort has been invested in the exhaustive classification of topological systems and a periodic table has been constructed categorising topological insulators and superconductors by their symmetries [4–7].

▶ Classification by the Ten-Fold Way

It is a nice exercise to classify the Kitaev chain according to the periodic table [4–7]. Therefore we need to study whether the BdG Hamiltonian (2.20) is invariant under certain symmetries, namely time-reversal $\mathcal{T}$, particle-hole C, and chiral symmetry S which is a combination of the two former ones. They are formally defined as

$$\begin{aligned} \mathcal{T}: &\quad U_T^\dagger H^* U_T = +H \\ C: &\quad U_C^\dagger H^T U_C = -H \\ S: &\quad U_S^\dagger H U_S = -H \quad , \quad U_S = U_C^* U_T^* \end{aligned}$$

Note that time-reversal and particle-hole are both *anti-unitary*.

In the Hilbert space of the Kitaev model the representations of the operators U_T and U_C are given by $U_T = \sigma^0$ and $U_C = \sigma^x$. For the BdG Hamiltonian (2.20) with complex order parameter $\Delta \in \mathbb{C}$ this means

$$\begin{aligned} \mathcal{T}: &\quad \sigma^0 H^*(-k)\sigma^0 \neq +H(k) \\ C: &\quad \sigma^x H^T(-k)\sigma^x = -H(k) \\ S: &\quad \sigma^x H(k)\sigma^x \neq -H(k) \end{aligned}$$

From this we infer that the Hamiltonian only fulfils the particle-hole symmetry. We can now proceed to look this up in the periodic table of topological insulators and superconductors in the column for spatial dimension $d = 1$ and find that the Kitaev chain belongs to class D which means that the topological invariant has $\mathbb{Z}_2$ character. Simply speaking the invariant can take two possible values indicating trivial or topological behaviour. This perfectly coincides with what we found for the winding number and the Majorana number.

2.1.5 Quantum Error Correction

We have promised to show how quantum error correction in the Kitaev model is achieved and here we will sketch the fundamentals to again bring the abstract calculations of the previous paragraphs into a greater picture. The exact algorithm is discussed in detail in [29].

Recall the Kitaev model at the ideal point (2.7), i.e. $t = -\Delta$ and $\mu = 0$, which we will henceforth refer to as $\hat{H}$.

$$\hat{H} = -it \sum_n \gamma_{2n}\gamma_{2n+1} \, .$$

In this form the two outermost Majoranas γ_1 and γ_{2N} remained unpaired and in particular—as these operators do not enter the Hamiltonian—they commute with $\hat{H}$. By combining them we can introduce a boundary mode b with occupation number operator n_b

$$b = \frac{1}{2}(\gamma_1 + i\gamma_{2N}) \quad \text{with} \quad n_b = b^\dagger b \, . \tag{2.35}$$

Because the boundary modes commute with $\hat{H}$ they are located perfectly at zero energy. The boundary mode is a fermionic mode, i.e. it has an occupation number $n_b = 0, 1$ but cannot be used as a qubit directly because the corresponding occupations $|0\rangle$ and $|1\rangle$ have different fermionic parity. One has to entangle the two modes with modes of the same parity from another system, e.g. a second Kitaev chain. Then we can encode a qubit into the state

$$|g\rangle = \alpha\,|0\rangle_1 \otimes |0\rangle_2 + \beta\,|1\rangle_1 \otimes |1\rangle_2 \, . \tag{2.36}$$

If we have encoded information in the qubit $|g\rangle$ we probably want to leave it there for some time and get coffee. While we enjoy our hot beverage the qubit is not idle and proceeds its time evolution according to the Schrödinger equation and after time t it has changed to $|g(t)\rangle = e^{iHt}\,|g\rangle$ where H is an *unknown* Hamiltonian which possibly introduces some errors. How can we recover the initially encoded state $|g\rangle$?

Before we begin, we will elucidate which kinds of errors this code is capable of correcting. Define the *stabilizer* operators S_n and *elementary errors* E_n

$$S_n = -i\gamma_{2n}\gamma_{2n+1} \quad \text{such that} \quad \hat{H} = t\sum_n S_n \,,$$
$$E_n = -i\gamma_{2n-1}\gamma_{2n} \,.$$

The unitary time evolution e^{iHt} can be decomposed into a superposition of errors $E = \gamma_{n_1}\cdots\gamma_{n_{2k}}$.

To correct an error, it has to be found first, which is done by a syndrome measurement Q_s. As mentioned earlier, a syndrome measurement is an eigenvalue measurement on all stabilizers which does not collapse the encoded qubit. Let s be the set of all measurement outcomes, then one can derive a suitable correction operator $C(s)$. There are several conditions to be met for the correction. First the corrected state must be part of the ground state space of $\hat{H}$. Second, only errors of small weight are captured, i.e. the error rate has to be small or the evolution time short. After these two operations we recover

$$C(s)Q_s \left|g(t)\right\rangle \sim (a_s I + b_s P)\left|g\right\rangle \,, \tag{2.37}$$

with the unity operator I, the parity operator P, and some amplitudes $a_s, b_s \in \mathbb{C}$. In [29] the authors also derive an expression for the fidelity of the storage for a stored bit $|g\rangle$ after some time t.

Before we conclude, a note on the unknown Hamiltonian H. For the above error correction algorithm to be successful it has to be well-behaved in the sense that it must not be non-Hermitian nor must it violate the fermionic parity (bit-flip errors of the encoded qubit).

Based on the discussions in [29] we briefly laid out how to encode a qubit in the boundary mode of a Kitaev chain and how potential errors can in principle be corrected. The fact that the topologically protected boundary modes are decoupled from the Hamiltonian (2.7) makes them robust against random local disorder.

2.1.6 Summary and Experimental Realisation

When the Majorana fermion was postulated it was envisioned as an elementary particle. A promising candidate for such a particle is the neutrino. Unfortunately, neutrinos interact only very weakly with other forms of matter and it has not yet been possible to verify the self-conjugateness of the neutrino.

Supersymmertic extensions to the Standard Model of elementary particles, also propose Majorana fermions as supersymmetric partners of the well-known gauge bosons. However, realisations are even more difficult to achieve here.

Kitaev [9] showed that a simple model involving superconductivity can host fermionic modes with the same properties as Majorana fermions. The modes are robust against disorder by topological protection and may thus provide a platform for quantum storage.

In 2012 Mourik *et al.* [26] reported for the first time that they had observed signatures of Majorana modes in semiconductor-superconductor heterostructures. The researchers found the electrical conductance to be peaked at zero voltage which corresponds to the zero bias peak in the local density of states in figure 2.3. Many other reports of findings of the same kind followed, for an overview see [30]. No experiments actually probing the Majorana character of these modes, i.e. self-conjugation or non-Abelian statistics, have been performed yet. It is a topic of ongoing research to realise wire networks of Kitaev chains (or equivalent systems) to perform the braiding.

2.2 Chiral p-wave Superconductor

Kitaev's Majorana chain is a one-dimensional model, therefore experimental realisations are constrained to nanowires and other one-dimensional structures which are hard to fabricate in the lab. It much easier to produce two-dimensional thin films, e.g. using evaporation techniques. The chiral p-wave superconductor is such a model system. Furthermore, it will serve as a playground for many of the numerical algorithms presented later because here we can compare the computations to known analytical results.

2.2.1 Basic Properties

The Kitaev model can be straightforwardly extended to two dimensions. Now the pairing is no longer solely p-wave but is extended to $p_x + ip_y$ or for short $p + ip$. The Hamiltonian simply reads

$$\begin{aligned} H = \sum_n & t(f_n^\dagger f_{n+x} + f_{n+x}^\dagger f_n) + t(f_n^\dagger f_{n+y} + f_{n+y}^\dagger f_n) - \mu f_n^\dagger f_n \\ & + (\Delta f_{n+x}^\dagger f_n^\dagger + \Delta^* f_n f_{n+x}) + (i\Delta f_{n+y}^\dagger f_n^\dagger - i\Delta^* f_n f_{n+y}) \,, \end{aligned} \tag{2.38}$$

where x and y are shorthands for a shift by the lattice unit vector in the corresponding direction.

In the following discussion we will not be so rigorous in the derivations as for the Kitaev chain, but will either point out where to find the precise steps or refer back to the previous section, since many of the methods simply stay the same. If the reader comes across these pages to learn about topological superconductivity it is instructive to perform all the intermediate steps oneself to build up some intuition. It also helps to better understand the later chapters.

We will start by transforming the Hamiltonian (2.38) to momentum space using the prescription (2.16) to obtain a BdG Hamiltonian as shown in section 2.1.3.

Using $\Psi_{\boldsymbol{k}} = (f_{\boldsymbol{k}}, f^\dagger_{-\boldsymbol{k}})^\top$ we find

$$H = \frac{1}{2}\sum_{\boldsymbol{k}} \Psi^\dagger_{\boldsymbol{k}} \begin{bmatrix} \xi(\boldsymbol{k}) & 2i\Delta(\sin k_x + i \sin k_y) \\ -2i\Delta^*(\sin k_x - i \sin k_y) & -\xi(\boldsymbol{k}) \end{bmatrix} \Psi_{\boldsymbol{k}} \,, \tag{2.39}$$

with the abbreviation $\xi(\boldsymbol{k}) = 2t(\cos k_x + \cos k_y) - \mu$. Just like for the Kitaev model we apply the gauge transformation (2.2) to get rid of the complex phase of the superconducting gap $\Delta \to |\Delta| e^{i\theta}$. Now we can write the Hamiltonian in terms of the Pauli matrices

$$H_{\boldsymbol{k}} = \xi(\boldsymbol{k})\sigma_z - 2|\Delta| \sin(k_x)\sigma_y - 2|\Delta| \sin(k_y)\sigma_x \,. \tag{2.40}$$

We have again recovered the form involving the $\boldsymbol{d}$ vector which determines the winding number

$$H_{\boldsymbol{k}} = \boldsymbol{d}(\boldsymbol{k}) \cdot \boldsymbol{\sigma} \quad \text{with} \quad \boldsymbol{d}(\boldsymbol{k}) = \begin{pmatrix} -2|\Delta| \sin(k_y) \\ -2|\Delta| \sin(k_x) \\ \xi(\boldsymbol{k}) \end{pmatrix} . \tag{2.41}$$

As is already known from (2.25) the energy eigenvalues of such a matrix are given by $E_\pm = \pm|\boldsymbol{d}(\boldsymbol{k})|$. We have thus extracted the excitation spectrum with minimal effort. To change between a trivial and a topological regime it is necessary that a gap closing takes place, which is the case for four distinct points (k_x, k_y, μ). The first critical point occurs at $(\pi, \pi, -4t)$. The second critical point is actually paired with the third one as they close the gap for same value of μ but at two different points in the Brillouin zone $(\pi, 0, 0)$ and $(0, \pi, 0)$. The last critical point is at $(0, 0, 4t)$. That is to say, we have four distinct phases namely for $\mu < -4t$, $-4t < \mu < 0$, $0 < \mu < 4t$, and $4t < \mu$, the first and the last one of which are trivial. The two others are topological phases with opposite chirality as defined by the spectral Chern number [31]

$$C = \frac{1}{8\pi} \int_{\mathrm{BZ}} \hat{\boldsymbol{d}} \cdot (\partial_{k_x} \hat{\boldsymbol{d}} \times \partial_{k_x} \hat{\boldsymbol{d}}) \mathrm{d}^2\boldsymbol{k} \,, \tag{2.42}$$

with the unit vector $\hat{\boldsymbol{d}} = \boldsymbol{d}/|\boldsymbol{d}|$. This is akin to the winding number in section 2.1.4. In the trivial phase with $|\mu| > 4|t|$ the vector $\hat{\boldsymbol{d}}$ does not cover the whole Bloch sphere contrary to the topological phases with $|\mu| < 4|t|$. Unfortunately, there exists no easy analytical expression for the winding number C. We will evaluate it seminumerically using a Gauß quadrature for the integration to compare it to the numerical algorithms for the Chern number, see appendix A.1.

2.2.2 Vortices and Majorana Fermions

In section 2.1.3 we have claimed that with the gap closing there is a change between trivial and topological phase taking place. This is only true when the

two regions cannot be smoothly deformed into each other by, say, avoiding the gap closing by taking another path. To elucidate what is happening at the transition, consider an interface between the two phases at the point $\mu = 4t$. The domain wall between the two phases is chosen along the k_y-direction whereas k_x points across the interface. The low energy physics takes place at $(k_x, k_y) = (0, 0)$, see above, so we can expand the lattice Hamiltonian around this point. For convenience we shift the chemical potential $\mu \to \bar{\mu} - 4t$

$$H_{\boldsymbol{k}} = \frac{1}{2}\begin{bmatrix} -\bar{\mu} & 2i\Delta(k_x + ik_y) \\ -2i\Delta^*(k_x^\dagger - ik_y^\dagger) & \bar{\mu} \end{bmatrix}, \tag{2.43}$$

where k_x and k_y are the momentum operators in canonical quantization. From this we can derive the BdG equations for a spinor $\psi = (u, v)^\top$. To this end we replace the operators k_x and k_y by their position representation and obtain

$$i\frac{\mathrm{d}u}{\mathrm{d}t} = -\bar{\mu}u + 2\Delta\left(\frac{\partial}{\partial x} + i\frac{\partial}{\partial y}\right)v\,, \tag{2.44}$$

$$i\frac{\mathrm{d}v}{\mathrm{d}t} = \bar{\mu}v + 2\Delta^*\left(\frac{\partial}{\partial x} - i\frac{\partial}{\partial y}\right)u\,. \tag{2.45}$$

This is compatible with $u = v^*$, indicating that the quasiparticles are their own antiparticles [32]. Because the interface postulated before is translationally invariant along one direction, k_y is still a good quantum number and can be plugged in for the operator

$$Eu = -\bar{\mu}u + 2\Delta\left(\frac{\partial}{\partial x} - k_y\right)v\,, \tag{2.46}$$

$$Ev = -2\Delta\left(\frac{\partial}{\partial x} + k_y\right)u + \bar{\mu}v\,. \tag{2.47}$$

The chemical potential $\bar{\mu}$ is chosen such that $\bar{\mu} > 0$ for $x < 0$ and $\bar{\mu} < 0$ for $x > 0$. Following after [32] we choose an ansatz for interface bound states

$$u(x) \propto \exp\left(-\frac{1}{2\Delta}\int_0^x \mu(x')\mathrm{d}x'\right), \tag{2.48}$$

where any phase factors have to be chosen such that $u = v^*$ is ensured. Given that Δ is real, we find $E = -2\Delta k_y$, i.e. there is a single bound state localised at the interface which goes to zero energy at $k_y = 0$.

We thus have found a Majorana bound state in the chiral p-wave superconductor at a domain wall between the trivial and the topological phase. Such a domain wall can be thought of as a one-dimensional cut through the system and can essentially be identified with a Kitaev chain. However, it was not initially clear that the Majorana state which can be hosted there is actually trapped.

The gap function of the chiral p-wave superconductor is momentum dependent. There are momenta for which the gap vanishes, i.e. the superconducting gap has nodes, which does not necessarily coincide with the bulk gap closing. At these nodes point sized domain walls form, so called *vortex cores*. We assume

that there exists a state at zero energy $E = 0$ at the vortex core. We put the vortex core to the origin of the coordinate system such that we can write the BdG equations in polar coordinates

$$2i\Delta e^{i\theta}\left(\frac{\partial}{\partial r} + \frac{i}{r}\frac{\partial}{\partial\theta}\right)v = \bar{\mu}u\,, \tag{2.49}$$

$$2i\Delta e^{-i\theta}\left(\frac{\partial}{\partial r} - \frac{i}{r}\frac{\partial}{\partial\theta}\right)u = -\bar{\mu}v\,, \tag{2.50}$$

with the ansatz from [32] where $f(r)$ is a real function

$$u(r,\theta) = \frac{1}{\sqrt{ire^{-i\theta}}}f(r)\,, \quad v(r,\theta) = \frac{1}{\sqrt{-ire^{i\theta}}}f(r) \tag{2.51}$$

the two BdG equations reduce to a single equation for $f(r)$, whose solution reads

$$f(r) \propto \exp\left(-\frac{1}{2\Delta}\int_0^r \mu(r')\mathrm{d}r'\right)\,. \tag{2.52}$$

This shows that Majorana bound states are pinned in the vortices of a $(p + ip)$-wave superconductor. These vortices can carry magnetic flux and are not necessarily pinned in location. This mobility leads to peculiar properties discussed below.

2.2.3 Non-Abelian Braiding Statistics

We have seen that there exist Majorana bound states in the vortices of a superconductor. Now we will examine what happens when we interchange these states, i.e. braid them [33]. Let $\gamma_0^{(n)}$ be the Majorana operator for the n-th vortex. Before we continue let us quickly discuss what happens when a particle moves around a vortex in a supercondutcor. A vortex carries the magnetic flux $\Phi_0 = hc/2e$ and a particle moving around it picks up the corresponding Aharanov-Bohm phase $e^{-ie\Phi_0} = -1$. That is to say, after having encircled a vortex the phase of the particle has switched its sign.

For periodic boundary conditions there cannot be only a single vortex because this would violate the overall flux conservation in case a magnetic flux is associated to it. Just like the Majorana fermions in the Kitaev chain they need to be paired up, e.g. according to (2.3). Here we define for two Majorana bound states $\gamma_0^{(1)}$ and $\gamma_0^{(2)}$

$$\gamma^\dagger = \frac{1}{\sqrt{2}}(\gamma_0^{(1)} + i\gamma_0^{(2)}) \quad \text{and} \quad \gamma = \frac{1}{\sqrt{2}}(\gamma_0^{(1)} - i\gamma_0^{(2)})\,. \tag{2.53}$$

Consider a pair of vortices with Majorana bound states $\gamma_0^{(1)}$ and $\gamma_0^{(2)}$. Let a third vortex $\gamma_0^{(3)}$ enter from infinity, encircle $\gamma_0^{(2)}$ and disappear again into the void. This vortex obviously has to have a partner but we consider this to stay

at infinity. The process of encircling is equivalent to exchanging vortices (1) and (2) twice [33]. If the Majorana bound states $\gamma_0^{(1)}$ and $\gamma_0^{(2)}$ were conventional fermions (or bosons) their final state after this process should be the same as the initial state before.

Consider an initial state $|i\rangle$ which is annihilated by the initial vortex configuration $\gamma\,|i\rangle = 0$. After encircling vortex (2) by vortex (3) both of them have switched signs. By this we also change the operator γ from above by

$$\gamma = \frac{1}{\sqrt{2}}(\gamma_0^{(1)} - i\gamma_0^{(2)}) \quad \rightarrow \quad \gamma = \frac{1}{\sqrt{2}}(\gamma_0^{(1)} + i\gamma_0^{(2)})\,. \tag{2.54}$$

This in turn means that the final state $|f\rangle$ is annihilated by $\gamma^\dagger\,|f\rangle = 0$ and is thus orthogonal to the initial state $\langle i|f\rangle = 0$. Such an exchange of two states can be described by a matrix (σ^x for a two level system).

Statistics which are described by a matrix are called *non-Abelian* statistics and particles obeying these are called non-Abelian anyons. This would allow to implement quantum gates and the process described above indeed corresponds to a NOT gate for qubits.

2.2.4 Chiral Edge States and Spontaneous Current

Earlier we found that there are bound states at interfaces in the $p + ip$-wave superconductor with a dispersion proportional to the edge momentum $E = -2\Delta k_y$. Obviously, the dispersion is not periodic which means that it will never reverse sign. That is to say, the bound state will travel along the edge in a single direction. This is the reason why the state is called *chiral*.

We can visualise this edge state in a calculation similar to the local density of states. We introduce the surface density of states (SDOS)

$$\rho_l(k_{\text{edge}}, E) = \sum_{m,\alpha} |\phi_\alpha^m(l, k_{\text{edge}})|^2 \delta(E - E_m) \approx -\operatorname{Im} \sum_{m,\alpha} \frac{|\phi_\alpha^m(l, k_{\text{edge}})|^2}{E - E_m + i\eta}\,, \tag{2.55}$$

where l stands for a layer parallel to the edge/interface, k_{edge} for the momentum along the edge and m runs over all eigenstates. The ϕ_α^m are the coefficients of the components of the resulting eigenvectors with energy eigenvalue E_m, where the index α denotes the degree of freedom (particle and hole for the chiral p-wave superconductor). Similar to the local density of states the δ distribution can be approximated by a Gaussian of finite width η.

There are two possible methods to calculate the SDOS. Either we diagonalise the real space Hamiltonian and Fourier transform the eigenvectors or we compute the spectrum for a Hamiltonian which is periodic along the edge direction. Using the second method it is much easier to extract the SDOS for $l = 0$ which we show in figure 2.6. The points are scaled and colour coded according to their spectral weight. There are two states leaping into the gap from the bulk (barely visible) which are not connected. This is the overlap from the other edge at

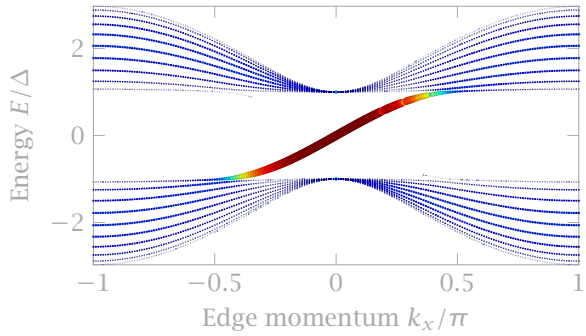

■ *Figure 2.6* Surface density of states in the chiral p-wave superconductor. The chiral state with Chern number $C = +1$ crosses through the gap and has linear dispersion around $k_x = 0$ as predicted. The points are scaled and coloured according to their spectral weight. Parameters are 201×10 sites, $l = 0$, $t = 1$, $\mu = 2$, $\Delta = 1$.

$l = N_y$.

According to Mahan [34] equation (1.202), the current density is defined as the time-derivative of the polarisation operator, which can be written as a commutator by Heisenberg's equation of motion

$$\boldsymbol{j} = \frac{\partial}{\partial t}\boldsymbol{P} = i[H, \boldsymbol{P}] \,, \tag{2.56}$$

where the polarisation operator is given by

$$\boldsymbol{P} = \sum_n \boldsymbol{r}_n n_n = \sum_{j,\sigma} \boldsymbol{r}_j c^\dagger_{j,\sigma} c_{j,\sigma} \,. \tag{2.57}$$

We calculate the current for (2.38). Carrying out the commutator is easy but tedious. We only present the result, split by vector components. Obviously, in a two-dimensional system there are only contributions in x- and y-direction.

$$j_x = it \sum_{n,\sigma} (f^\dagger_{n,\sigma} f_{n+x,\sigma} - f^\dagger_{n+x,\sigma} f_{n,\sigma}) \,, \tag{2.58}$$

$$j_y = it \sum_{n,\sigma} (f^\dagger_{n,\sigma} f_{n+y,\sigma} - f^\dagger_{n+y,\sigma} f_{n,\sigma}) \,. \tag{2.59}$$

For the surface density of states we chose the edge to be along the x-direction. To this end we also present the current resolved by the edge momentum. Therefore we Fourier transform the expression for j_x only in x-direction.

$$j_x = -2t \sum_{k_x,j,\sigma} \sin k_x \, f^\dagger_{k_x,j,\sigma} f_{k_x,j,\sigma} \,. \tag{2.60}$$

In figure 2.7 we plot the real space current and the k-space current. The real space current was computed for a system with 20×10 and open boundary conditions. The vectors indicate that the current is going around the system. The magnitude is colour coded where red means stronger. The k-space current

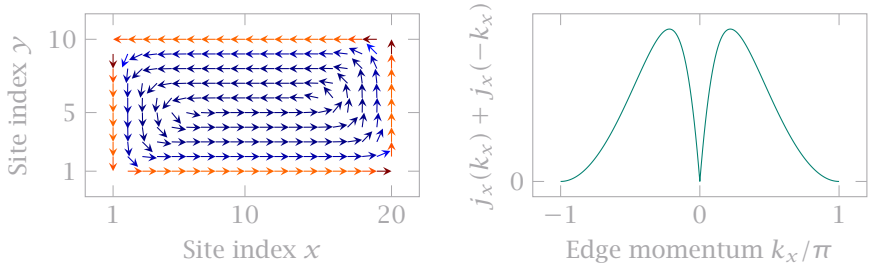

■ *Figure 2.7* We show the expectation value of the current operator. On the *left-hand side* we plot the current density in real space with vectors for 20×10 sites with open boundary conditions. One can clearly see the current going around the system. On the *right-hand side* we plot the symmetrised current of the layer $l = 0$ for 101×10 sites with periodic boundary conditions along the edge. Parameters are $t = 1$, $\mu = 2$, $\Delta = 1$.

was computed for a system with 101×10 sites and periodic boundary conditions in x-direction. The signal in this edge momentum resolved current is mainly dominated by the asymmetric sine function. To extract the signal emergent form the chiral edge state we symmetrise it using $j_x(k_x) + j_x(-k)$ such that the asymmetric part drops out.

2.3 Engineering Topological Superconductivity

The models we have introduced so far have the drawback that they are spinless. If we would promote these models to a spinful description they would be pairing up electrons of the same spin. There exist unconventional superconductors with such a pairing mechanism but they are very rare in nature and have not yet been observed experimentally, though candidate materials such as Sr_2RuO_4 have been identified [35].

Therefore it is of great interest to engineer an *effective* p-wave pairing in conventional superconductors. To this end the degeneracy of the two spin directions has to be lifted which is possible by applying a magnetic field. Unfortunately, this breaks the pairing process in the first place because electrons of opposite spins at the Fermi surface have to be paired up which is no longer possible if their Fermi surfaces are separated by an energy splitting. This problem can be circumvented by not considering an external magnetic field but magnetic adatoms whose magnetisation varies locally [11, 12, 14, 36]. If this variation is chosen in a certain way it is possible for the system to stabilise Majorana edge states. The same effect can also be achieved using magnetic adatoms with ferromagnetic ordering and spin–orbit coupling in the superconductor [15,37, 38].

Summary of Chapter 2

Kitaev's Majorana chain [9] provides a simple toy model for a topological superconductor in one dimension. It is described by a simple tight-binding Hamiltonian (2.1) with the three parameters hopping, pairing, and chemical potential. By transforming it to a representation involving Majorana operators (2.3) one can show that for certain choices of the parameters unpaired Majorana fermions arise at the end of the system.

After Fourier transforming using (2.16), the Hamiltonian can be written in Bogoliubov-de-Gennes form (2.20) from which we can extract the bulk excitation spectrum and the topological invariant which is in this case given by a winding number (2.26). Alternatively, one could also extract the Majorana number (2.33) which is a property of the Hamiltonian itself rather than the wave function and is given in terms of the Pfaffian of the Hamiltonian in the Majorana basis.

Majorana fermions cannot really exist unpaired because they only correspond to *half* a physical fermion. In the case of the two unpaired Majorana fermions they have to be paired up over the whole system which gives them a non-local nature. This non-locality in turn makes them very robust to local perturbations and good candidates for building blocks in a quantum storage device.

The chiral p-wave superconductor can be seen as a Kitaev model promoted to two dimensions (2.38). From the Bogoliubov-de-Gennes form of the Hamiltonian a topological invariant similar to the winding number can be extracted (A.1). A magnetic field pierces the superconductor leading to vortices. The vortex core traps a single Majorana zero mode and braiding two vortices reveals their non-Abelian statistics.

Chapter 3

Magnetic Adatoms

Intrinsic topological superconductors are rare in nature, because they require unconventional pairing mechanisms such as $(p_x + ip_y)$-wave. Kitaev [9] showed that fermionic Majorana modes can be found in one-dimensional p-wave superconducting chains.

Instead of relying on intrinsic topological superconductivity of materials it has been proposed to induce an *effective* p-wave pairing state by coupling a conventional s-wave superconductor to a chain of magnetic adatoms [11, 12, 14, 36]. The existence of a topological phase with Majorana edge modes depends on the alignment of the spins of the magnetic adatoms. An alternative approach is to exploit spin–orbit coupling in superconductors in conjunction with ferromagnetic adatoms [15], which has been realised experimentally [13] with great success.

3.1 Shiba States

Impurities in superconductors give rise to bound states in the gap [39]. These sub-gap states were first introduced by Yu [40], Shiba [41], and Rusinov [42] and are thus usually called Yu-Shiba-Rusinov states or only Shiba states.

Consider magnetic impurities deposited on the surface of a superconductor. The impurities are given by classical spins which couple to the quasiparticle spin located at the same position via a Zeeman (or Stern-Gerlach) term

$$H_{\text{imp}} = \int \mathrm{d}\boldsymbol{r}\, \Psi^\dagger_\alpha(\boldsymbol{r})(\boldsymbol{B}(\boldsymbol{r}) \cdot \boldsymbol{\sigma}_{\alpha\beta})\Psi_\beta(\boldsymbol{r})\,. \tag{3.1}$$

In the case of a single impurity at the origin of the coordinate system $B(\boldsymbol{r}) = \boldsymbol{B}\delta(\boldsymbol{r})$ Shiba originally derived the bound state energy as

$$E_0 = \frac{1 - (B\pi N_0/2)^2}{1 + (B\pi N_0/2)^2}\Delta\,, \tag{3.2}$$

where N_0 is the normal state density of states at the Fermi energy. The wavefunctions of the Shiba bound states can be computed from the Bogoliubov-de-Gennes equations and decay into the bulk. In the case of many impurities with tight spacing these decaying bound states overlap and form bands. For certain con-

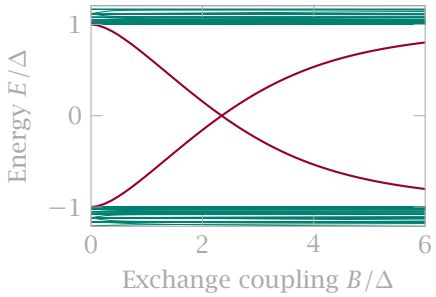

■ *Figure 3.1* We show the spectrum for a single impurity with exchange coupling B in a superconductor with 20×20 sites and periodic boundary conditions. There is a bound state for each of the two spin directions (coloured in red). The bulk bands are coloured in green. For a critical value B_c of the exchange coupling the lines intersect. Parameters are $t = 1$, $\mu = 0.5$, $\Delta = 1$.

figurations which we will discuss later, this band structure exhibits non-trivial topology.

To derive the above result analytically is quite hard. The full derivation is given in the paper by Yu [40]. We can still reproduce the result by performing a tight-binding calculation on the following Hamiltonian

$$H = t \sum_{n,\sigma} (f^\dagger_{n,\sigma} f_{n+1,\sigma} + \text{H.c.}) - \mu \sum_{n,\sigma} f^\dagger_{n,\sigma} f_{n,\sigma} + \Delta \sum_n (f^\dagger_{n,\uparrow} f^\dagger_{n,\downarrow} + f_{n,\downarrow} f_{n,\uparrow}) + H_{\text{imp}} \,. \tag{3.3}$$

The hopping and chemical potential term are already known from the Kitaev chain but now we have an additional spin degree of freedom. The pairing is now on-site and pairs up different spin directions. This is known as a conventional s-wave superconductor.

The original result by Shiba was obtained in periodic boundary conditions which we also impose on our tight-binding model. We diagonalise the Hamiltonian on a 20×20 lattice for different values of B with the impurity located at the centre. The resulting spectrum is shown in figure 3.1. We find two bound states in the gap, one for each spin direction. For a critical value B_c of the exchange coupling the associated lines intersect at zero energy. The band inversion at this point already indicates topological features. The question is how to pin the subgap state at zero energy over a larger interval of B. The first thought of course is to add more impurities to have more subgap states. Unfortunately, ferromagnetic impurities suppress superconductivity which is the reason for the bound state in the first place. This drawback can be remedied by the introduction of either a helical ordering of the attached impurities or spin–orbit coupling in the superconductor [11–15,36].

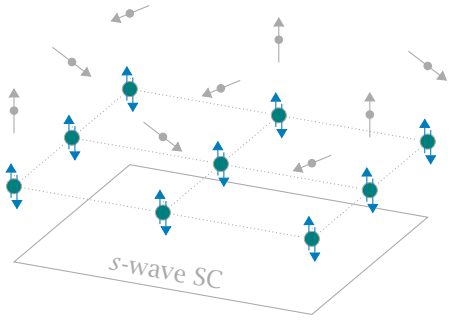

Figure 3.2 Sketch of the system proposed by Nakosai *et al.* [43]. A two-dimensional structure with *s*-wave Cooper pairing interacts with a spin texture, which induces a magnetic interaction.

3.2 Spin Texture

As already pointed out, topological superconductivity can be realised in heterostructures with magnetic adatoms of specific alignment. The structure of this magnetic coupling is imprinted via a spin texture on top of the lattice. The impurity Hamiltonian is then site dependent [43]

$$H = t\sum_{n,\sigma}(f^\dagger_{n,\sigma}f_{n+1,\sigma} + \text{H.c.}) - \mu\sum_{n,\sigma} f^\dagger_{n,\sigma}f_{n,\sigma} + \Delta\sum_n (f^\dagger_{n,\uparrow}f^\dagger_{n,\downarrow} + f_{n,\downarrow}f_{n,\uparrow}) + \sum_{n,\alpha,\beta}(\boldsymbol{B}_n\cdot\boldsymbol{\sigma})_{\alpha\beta}f^\dagger_{n,\alpha}f_{n,\beta}\,. \quad (3.4)$$

A sketch of a candidate system implementing this Hamiltonian is depicted in figure 3.2.

Transforming the Hamiltonian (3.4) to k-space is not feasible for a general spin configuration, as the spin texture $\{\boldsymbol{B}_n\}$ eludes itself from a straightforward Fourier transformation. Usually the classical spins are taken to have the same coupling strength at all sites and are parametrised by spherical coordinates

$$\boldsymbol{B}_n(\theta,\phi) = B(\sin\theta_n\cos\phi_n, \sin\theta_n\sin\phi_n, \cos\theta_n)\,. \quad (3.5)$$

Interactions among the impurity spins are induced by exchange processes, such as the Ruderman-Kittel-Kasuya-Yosida (RKKY) [44–46] interaction or Dzyaloshinskii-Moriya interaction [47,48]. It is not a priori clear which kind of ordering of the adatoms is preferred. It has been observed that ferromagnetic ordering is favoured in tightly packed chains of adatoms [13]. Other studies [49,50] suggest that a ferromagnetic order is not stable in the superconducting state and helical patterns, e.g. a spiral are favoured. We will therefore investigate both in the following text.

3.3 Spin–Orbit Coupling in Solid State Physics

Brydon *et al.* [15] proposed a two-dimensional *s*-wave superconductor with Rashba spin–orbit coupling. The authors showed that it is feasible to realise a topological state of the subgap band formed by magnetic impurities in the presence of Rashba spin–orbit coupling. Spin-flip correlations emerging from the spin–orbit coupling lead to a topological phase for ferromagnetic order of the magnetic impurities.

The Hamiltonian in [15] is given in the BdG form $H = \sum_{\boldsymbol{k}} \Psi_{\boldsymbol{k}}^\dagger H_{\boldsymbol{k}} \Psi_{\boldsymbol{k}}$ where

$$H_{\boldsymbol{k}} = \xi_{\boldsymbol{k}} \tau_z \otimes \sigma_0 + \tau_z \otimes (\boldsymbol{l}_{\boldsymbol{k}} \cdot \boldsymbol{\sigma}) + \Delta \tau_x \otimes \sigma_0 \,, \tag{3.6}$$

where the first and the last term describe the bare *s*-wave superconductor, whereas the second term represents the spin–orbit coupling.

The Nambu space is spanned by $\Psi_{\boldsymbol{k}} = (f_{\boldsymbol{k},\uparrow}, f_{\boldsymbol{k},\downarrow}, f^\dagger_{-\boldsymbol{k},\uparrow}, -f^\dagger_{-\boldsymbol{k},\downarrow})$ and the Rashba spin–orbit coupling is parametrised by $\boldsymbol{l}_{\boldsymbol{k}} = \lambda(k_y \boldsymbol{e}_x - k_x \boldsymbol{e}_y)$. To derive this form of the spin–orbit coupling one has to take into account symmetry constraints. These are time-reversal symmetry and the crystallographic point group symmetry of the material. Time-reversal symmetry demands that $\boldsymbol{l}_{\boldsymbol{k}}$ is odd in $\boldsymbol{k}$. An element from the crystallographic point group can be either a proper rotation ($\det R = 1$) or an improper rotation ($\det R = -1$). One then has

$$\boldsymbol{l}_{\boldsymbol{k}} = \det(R) R \boldsymbol{l}_{R^{-1}\boldsymbol{k}} \,. \tag{3.7}$$

A small-momentum expansion (nearest neighbour approximation) for the tetragonal point group $\mathcal{G} = C_{4v}$ then yields [51]

$$\boldsymbol{l}_{\boldsymbol{k}} = \lambda(k_y \boldsymbol{e}_x - k_x \boldsymbol{e}_y) \,. \tag{3.8}$$

An extensive table for a myriad of point and line groups and several orders of expansion is given by Samokhin [51].

To consider a finite system, which is crucial for the existence of an edge state, we need to transform the spin–orbit coupling to real space. Therefore, we proceed to multiply out the spin–orbit coupling term in the Nambu space and are left with

$$H^{\mathrm{SOC}} = \boldsymbol{l}_{\boldsymbol{k}} \cdot \boldsymbol{\sigma} = 2\lambda \sum_{\boldsymbol{k}} (k_y + i k_x) f^\dagger_{\boldsymbol{k},\uparrow} f_{\boldsymbol{k},\downarrow} + \mathrm{H.c.} \tag{3.9}$$

To be able to Fourier transform this representation to real space we assume the lattice form of the Rashba-type SOC, i.e. $k_\mu \to \sin k_\mu$. With this one finds

$$H^{\mathrm{SOC}} = 2\lambda \sum_{\boldsymbol{k}} (\sin k_y + i \sin k_x) f^\dagger_{\boldsymbol{k},\uparrow} f_{\boldsymbol{k},\downarrow} + (\sin k_y - i \sin k_x) f^\dagger_{\boldsymbol{k},\downarrow} f_{\boldsymbol{k},\uparrow} \,. \tag{3.10}$$

The complete process of the Fourier transformation is straightforward. Here, we only present the result, which reads

$$H^{\mathrm{SOC}} = \lambda \sum_n [(f^\dagger_{n-x,\downarrow} f_{n,\uparrow} - f^\dagger_{n+x,\downarrow} f_{n,\uparrow}) + i(f^\dagger_{n-y,\downarrow} f_{n,\uparrow} - f^\dagger_{n+y,\downarrow} f_{n,\uparrow}) + \mathrm{H.c.}] \,. \tag{3.11}$$

We immediately see that there is an anisotropy present, which is an *imaginary* coupling in y-direction as opposed to a real coupling in x-direction.

With spin–orbit coupling the Hamiltonian (3.4) becomes

$$\begin{aligned} H = t \sum_{n,\sigma} (f^\dagger_{n,\sigma} f_{n+1,\sigma} + \mathrm{H.c.}) - \mu \sum_{n,\sigma} f^\dagger_{n,\sigma} f_{n,\sigma} + \Delta \sum_n (f^\dagger_{n,\uparrow} f^\dagger_{n,\downarrow} + f_{n,\downarrow} f_{n,\uparrow}) \\ + \lambda \sum_n [(f^\dagger_{n-\boldsymbol{\delta}_x,\downarrow} f_{n,\uparrow} - f^\dagger_{n+\boldsymbol{\delta}_x,\downarrow} f_{n,\uparrow}) + i(f^\dagger_{n-\boldsymbol{\delta}_y,\downarrow} f_{n,\uparrow} - f^\dagger_{n+\boldsymbol{\delta}_y,\downarrow} f_{n,\uparrow}) + \mathrm{H.c.}] \\ + \sum_{n,\alpha,\beta} (\boldsymbol{B}_n \cdot \boldsymbol{\sigma})_{\alpha\beta} f^\dagger_{n,\alpha} f_{n,\beta} \end{aligned} \tag{3.12}$$

3.4 Topological Phases in a Shiba Chain

We start by summarizing some results given in [12] where a helical magnet on an s-wave superconductor is considered. In a next step we show that this model is unitarily equivalent to a ferromagnet on an s-wave superconductor with intrinsic spin–orbit coupling. Last, we extend the model given in [12] by considering a helical magnet in conjunction with spin–orbit coupling.

3.4.1 Helical Spin Texture

The chain with magnetic impurities is quite similar to the Kitaev chain in the sense that it also belongs to class D according to the ten-fold way of classification [4–7]. The host superconductor ensures particle-hole symmetry whereas the magnetic field from the adatoms breaks time-reversal symmetry. For a one-dimensional system the topological invariant is given by the Pfaffian of the Hamiltonian in a Majorana basis. Nadj-Perge *et al.* [12] evaluated the Pfaffian for a one-dimensional chain with the magnetic impurities adjusted in a spiral, akin to figure 3.2. They parametrised the orientation of the magnetic impurities as in (3.5) and applied a unitary transformation to rotate this orientation locally to point along the z-axis. We briefly summarise their results for later comparison. The Hamiltonian in [12] reads

$$\begin{aligned} H = \sum_{n,\alpha} (t f^\dagger_{n,\alpha} f_{n+1,\alpha} + \mathrm{H.c.}) - \mu \sum_{n,\alpha} f^\dagger_{n,\alpha} f_{n,\alpha} + \sum_n (\Delta_n f^\dagger_{n,\uparrow} f^\dagger_{n,\downarrow} + \mathrm{H.c.}) \\ + \sum_{n,\alpha,\beta} (\boldsymbol{B}_n \cdot \boldsymbol{\sigma})_{\alpha\beta} f^\dagger_{n,\alpha} f_{n,\beta} \,. \end{aligned} \tag{3.13}$$

The local gap parameter Δ_n is set globally to a constant Δ_0. As already mentioned, the magnetic impurities are parametrised by

$$\boldsymbol{B}_n = B_0(\sin\theta_n\cos\phi_n, \sin\theta_n\sin\phi_n, \cos\theta_n)^\top .$$

The unitary transformation is constructed from the product of three rotations in spin space. The common rotation is given by

$$R_n(\alpha) = \exp\left(i\frac{\alpha}{2}\boldsymbol{n}\cdot\boldsymbol{\sigma}\right) = \sigma_0\cos\left(\frac{\alpha}{2}\right) + i(\boldsymbol{n}\cdot\boldsymbol{\sigma})\sin\left(\frac{\alpha}{2}\right) \tag{3.14}$$

with the axis of rotation $\boldsymbol{n}$ and the angle of rotation α. We then rotate

$$U_n = R_z(-\phi_n)\cdot R_y(-\theta_n)\cdot R_z(\phi_n) = \begin{bmatrix} \cos\theta_n/2 & -\sin\theta_n/2\, e^{-i\phi_n} \\ \sin\theta_n/2\, e^{i\phi_n} & \cos\theta_n/2 \end{bmatrix}. \tag{3.15}$$

This transformation is applied to the fermionic operators $f_{n,\sigma}$, such that

$$\begin{pmatrix} f_{n,\uparrow} \\ f_{n,\downarrow} \end{pmatrix} = U_n \begin{pmatrix} g_{n,\uparrow} \\ g_{n,\downarrow} \end{pmatrix}, \tag{3.16}$$

with the new operators $g_{n,\sigma}$. Since the transformation is unitary, the commutation relations are not affected and $g_{n,\sigma}$ are again fermionic operators. The transformation does not change the form of the chemical potential and gap term in (3.13), but the exchange coupling becomes diagonal and the hopping acquires components mixing the spins

$$\begin{aligned} H = \sum_{n,\alpha,\beta} t\Omega_{n,\alpha,\beta} g^\dagger_{n,\alpha} g_{n+1,\beta} + t^*\Omega^*_{n,\beta,\alpha} g^\dagger_{n+1,\alpha} g_{n,\beta} + B_0\sigma_{z,\alpha\beta} g^\dagger_{n,\alpha} g_{n,\beta} \\ - \mu\sum_{n,\alpha} g^\dagger_{n,\alpha} g_{n,\alpha} + \sum_n \Delta_0 (g^\dagger_{n,\uparrow} g^\dagger_{n,\downarrow} + g_{n,\downarrow} g_{n,\uparrow}) , \end{aligned} \tag{3.17}$$

with the matrix Ω_n

$$\Omega_n = \begin{bmatrix} \alpha_n & -\beta^*_n \\ \beta_n & \alpha^*_n \end{bmatrix}, \tag{3.18}$$

whose elements α_n and β_n are given in [12] by

$$\alpha_n = \cos\frac{\theta_n}{2}\cos\frac{\theta_{n+1}}{2} + \sin\frac{\theta_n}{2}\sin\frac{\theta_{n+1}}{2} e^{-i(\phi_n-\phi_{n+1})} , \tag{3.19}$$

$$\beta_n = -\sin\frac{\theta_n}{2}\cos\frac{\theta_{n+1}}{2} e^{i\phi_n} + \cos\frac{\theta_n}{2}\sin\frac{\theta_{n+1}}{2} e^{i\phi_{n+1}} . \tag{3.20}$$

For a static angle $\theta = \theta_{n+1} - \theta_n$ between adjacent sites and $\phi_n = 0$ the matrix elements reduce to $\alpha = \cos\theta/2$ and $\beta = \sin\theta/2$. Such a spiral is illustrated in figure 3.3.

However, θ is initially not constrained and therefore $\theta \in [0, 2\pi)$. It is important to note that even though we find a topological invariant indicating

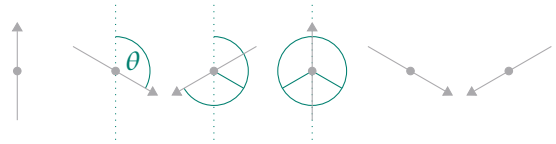

■ *Figure 3.3* The classical spins are ordered in a helical pattern with periodicity of the full spiral $n\theta = 2\pi$, here we have $n = 3$. By unitary transformation this spin texture can be made commensurate with the lattice.

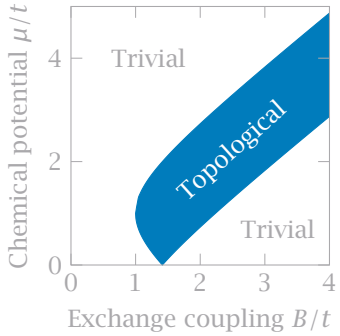

■ *Figure 3.4* Topological phase diagram from the analytical expression (3.22). Parameters are $t = 1$, $\Delta = 1$, $\theta = 2\pi/3$.

non-trivial behaviour for all θ the bulk spectrum is *not* always gapped. We want to stress again that both conditions have to be met simultaneously to give rise to topologically protected states in non-interacting systems.

After expressing the above Hamiltonian (3.17) in the Majorana basis and transforming to k-space Nadj-Perge *et al.* [12] find for the Pfaffian

$$\mathrm{Pf}[A(q)] = B_0^2 - [\mu - 2t\alpha\cos(q)]^2 - [\Delta_0 - 2it\beta\sin(q)]^2 \tag{3.21}$$

and derive the following condition for the topological phase

$$\sqrt{\Delta_0^2 + (|\mu| + |2\alpha t|)^2} > B_0 > \sqrt{\Delta_0^2 + (|\mu| - |2\alpha t|)^2}\,. \tag{3.22}$$

Finally we show a topological phase diagram illustrating this condition in figure 3.4.

3.4.2 Ferromagnetic Spin Texture with Spin–Orbit Coupling

We now want to show that the effects of a helical magnet can be related to those of Rashba-type spin–orbit coupling. We will thus compute the Pfaffian for a model similar to the one in [12] but with the magnetic impurities in ferromagnetic ordering (all aligned in the same direction) and an additional spin–orbit coupling term. The Majorana transformation is given by (2.3)

$$\gamma_{2n-1,\sigma} = f_{n,\sigma} + f_{n,\sigma}^\dagger \,, \quad \gamma_{2n,\sigma} = -i(f_{n,\sigma} - f_{n,\sigma}^\dagger)$$

with the properties

$$\gamma_{n,\sigma}^\dagger = \gamma_{n,\sigma} \,, \quad \{\gamma_{n,\sigma}, \gamma_{m,\sigma'}\} = 2\delta_{n,m}\delta_{\sigma,\sigma'}$$

and vice versa

$$f_{n,\sigma} = \frac{1}{2}(\gamma_{2n-1,\sigma} + i\gamma_{2n,\sigma}) \,, \quad f_{n,\sigma}^\dagger = \frac{1}{2}(\gamma_{2n-1,\sigma} - i\gamma_{2n,\sigma}) \,.$$

We use these substitution rules to obtain the Majorana representation of (3.13), which is also given in [12] as

$$\begin{aligned} H = &\sum_{n,\sigma} \frac{i\,\mathrm{Re}(t_n)}{2}(\gamma_{2n-1,\sigma}\gamma_{2n+2,\sigma} - \gamma_{2n,\sigma}\gamma_{2n+1,\sigma}) \\ &+ \frac{i\,\mathrm{Im}(t_n)}{2}(\gamma_{2n-1,\sigma}\gamma_{2n+1,\sigma} + \gamma_{2n,\sigma}\gamma_{2n+2,\sigma}) - \frac{i\mu}{2}\gamma_{2n-1,\sigma}\gamma_{2n,\sigma} \\ &+ \sum_n \frac{iB_{n,x}}{2}(\gamma_{2n-1,\uparrow}\gamma_{2n,\downarrow} - \gamma_{2n,\uparrow}\gamma_{2n-1,\downarrow}) - \frac{iB_{n,y}}{2}(\gamma_{2n-1,\uparrow}\gamma_{2n-1,\downarrow} + \gamma_{2n,\uparrow}\gamma_{2n,\downarrow}) \\ &+ \frac{iB_{n,z}}{2}(\gamma_{2n-1,\uparrow}\gamma_{2n,\uparrow} - \gamma_{2n-1,\downarrow}\gamma_{2n,\downarrow}) + \frac{i\Delta_0}{2}(\gamma_{2n-1,\downarrow}\gamma_{2n,\uparrow} + \gamma_{2n,\downarrow}\gamma_{2n-1,\uparrow}) \,. \end{aligned} \tag{3.23}$$

For simplicity and to compare with the model (3.12) in ferromagnetic order, we adjust the parameters in the above equation:

$$\boldsymbol{B}_n \to \boldsymbol{B} \,, \quad t_n \to t' \,, \quad t' \in \mathbb{R} \,.$$

Furthermore, we add the spin–orbit coupling term (3.11), where we cancel all the terms containing hopping in y-direction, since we are looking at a 1D chain. The Majorana representation reads

$$H^{\mathrm{SOC}} = \sum_n \frac{i\lambda}{2}(\gamma_{2n+2,\downarrow}\gamma_{2n-1,\uparrow} + \gamma_{2n,\uparrow}\gamma_{2n+1,\downarrow} + \gamma_{2n-1,\uparrow}\gamma_{2n-2,\downarrow} + \gamma_{2n-3,\downarrow}\gamma_{2n,\uparrow}) \,. \tag{3.24}$$

The full Hamiltonian in Majorana form thus reads

$$\begin{aligned} H = &\sum_{n,\sigma} \frac{it'}{2}(\gamma_{2n-1,\sigma}\gamma_{2n+2,\sigma} - \gamma_{2n,\sigma}\gamma_{2n+1,\sigma}) - \frac{i\mu}{2}\gamma_{2n-1,\sigma}\gamma_{2n,\sigma} \\ &+ \sum_n \frac{iB_x}{2}(\gamma_{2n-1,\uparrow}\gamma_{2n,\downarrow} - \gamma_{2n,\uparrow}\gamma_{2n-1,\downarrow}) - \frac{iB_y}{2}(\gamma_{2n-1,\uparrow}\gamma_{2n-1,\downarrow} + \gamma_{2n,\uparrow}\gamma_{2n,\downarrow}) \\ &+ \frac{iB_z}{2}(\gamma_{2n-1,\uparrow}\gamma_{2n,\uparrow} - \gamma_{2n-1,\downarrow}\gamma_{2n,\downarrow}) + \frac{i\Delta_0}{2}(\gamma_{2n-1,\downarrow}\gamma_{2n,\uparrow} + \gamma_{2n,\downarrow}\gamma_{2n-1,\uparrow}) \\ &+ \frac{i\lambda}{2}(\gamma_{2n+2,\downarrow}\gamma_{2n-1,\uparrow} + \gamma_{2n,\uparrow}\gamma_{2n+1,\downarrow} + \gamma_{2n-1,\uparrow}\gamma_{2n-2,\downarrow} + \gamma_{2n-3,\downarrow}\gamma_{2n,\uparrow}) \,. \end{aligned} \tag{3.25}$$

Now we Fourier transform this result using the prescription

$$\gamma_{2n-1,\sigma} = \frac{1}{\sqrt{N}} \sum_q e^{-iqn} b_{q,1,\sigma} \ , \quad \gamma_{2n,\sigma} = \frac{1}{\sqrt{N}} \sum_q e^{-iqn} b_{q,2,\sigma} \ . \tag{3.26}$$

Note, that $b_q^\dagger = b_{-q}$. We obtain the form

$$H = \frac{i}{4} \sum_q b_q^\dagger A(q) b_q \ , \tag{3.27}$$

with $b_q = (b_{q,1,\uparrow}, b_{q,1,\downarrow}, b_{q,2,\uparrow}, b_{q,2,\downarrow})^\top$ and the skew-symmetric matrix $A(q)$. The non-zero elements of $A(q)$ are given by

$$\begin{aligned} A_{12} &= -B_y & A_{23} &= \Delta_0 + 2i\lambda \sin(-q) + B_x \\ A_{13} &= 2t' \cos(q) - \mu + B_z & A_{24} &= 2t' \cos(q) - \mu - B_z \\ A_{14} &= B_x + 2i\lambda \sin(q) - \Delta_0 & A_{34} &= -B_y \end{aligned} \tag{3.28}$$

The Pfaffian of this 4×4-matrix is hence

$$\mathrm{Pf}[A(q)] = |\boldsymbol{B}|^2 - [\mu - 2t' \cos(q)]^2 - [\Delta_0 - 2i\lambda \sin(q)]^2 \ . \tag{3.29}$$

By a direct comparison with (3.21) one finds

$$t' = t \cos\theta/2 \ , \quad \lambda = t \sin\theta/2 \ . \tag{3.30}$$

The system under consideration belongs to class D according to the periodic table of topological insulators and superconductors [4–7]. In one spatial dimension the topological invariant is of $\mathbb{Z}_2$ character. From (3.29) we can determine this bulk $\mathbb{Z}_2$ invariant, which is the Majorana number (as for the Kitaev chain) and is given by

$$W = \prod_a \frac{\mathrm{Pf}[A(\Lambda_a)]}{\sqrt{\det[A(\Lambda_a)]}} = \prod_a \mathrm{sgn}(\mathrm{Pf}[A(\Lambda_a)]) = \pm 1 \tag{3.31}$$

where $\mathrm{sgn}(\cdot)$ is the signum function and Λ_a are the time-reversal invariant momenta, here $\Lambda_a \in \{0, \pi\}$. Working out W reads

$$\begin{aligned} &\mathrm{sgn}(\mathrm{Pf}[A(0)]) \, \mathrm{sgn}(\mathrm{Pf}[A(\pi)]) \\ &\quad = \mathrm{sgn}(|\boldsymbol{B}|^2 - (\mu - 2t')^2 - \Delta_0^2) \, \mathrm{sgn}(|\boldsymbol{B}|^2 - (\mu + 2t')^2 - \Delta_0^2) \ , \end{aligned} \tag{3.32}$$

which has to be equal to -1. This is indeed fulfilled for

$$\sqrt{\Delta_0^2 + (|\mu| + |2t'|)^2} > |\boldsymbol{B}| > \sqrt{\Delta_0^2 + (|\mu| - |2t'|)^2} \ . \tag{3.33}$$

This is in essence the same condition as (3.22) and again implies $|t'| = |\alpha t|$.

3.4.3 Helical Spin Texture with Spin–Orbit Coupling

In the previous paragraph we have shown that there exists a correspondence between the helical spin texture and a ferromagnetic spin texture with spin–orbit coupling. Both exhibit topological phases and for the choice of parameters (3.30) their topological phase diagram is identical.

The question remains, whether for a helical spin texture the presence of spin–orbit coupling immediately spoils the topological regime. To this end we again build upon the result from [12]. We need to rotate the spin–orbit coupling term (3.11) with the same transformation as (3.17). This way, spin–orbit coupling in the k_x-direction transforms like

$$\sum_n (f^\dagger_{n-1,\downarrow} f_{n,\uparrow} - f^\dagger_{n+1,\downarrow} f_{n,\uparrow}) + (f^\dagger_{n,\uparrow} f_{n-1,\downarrow} - f^\dagger_{n,\uparrow} f_{n+1,\downarrow}) \\ = \sum_{n,\alpha,\beta} \bar{\Omega}_{n,\alpha,\beta} g^\dagger_{n,\alpha} g_{n+1,\beta} + \bar{\Omega}^*_{n,\beta,\alpha} g^\dagger_{n+1,\alpha} g_{n,\beta} \,, \tag{3.34}$$

with the matrix $\bar{\Omega}_n$

$$\bar{\Omega}_n = \begin{bmatrix} -\bar{\beta}^*_n & -\bar{\alpha}_n \\ \bar{\alpha}^*_n & -\bar{\beta}_n \end{bmatrix}, \tag{3.35}$$

which elements $\bar{\alpha}_n$ and $\bar{\beta}_n$ are given by

$$\bar{\alpha}_n = \cos\frac{\theta_n}{2}\cos\frac{\theta_{n+1}}{2} + \sin\frac{\theta_n}{2}\sin\frac{\theta_{n+1}}{2} e^{-i(\phi_n+\phi_{n+1})} \,, \tag{3.36}$$

$$\bar{\beta}_n = -\sin\frac{\theta_n}{2}\cos\frac{\theta_{n+1}}{2} e^{i\phi_n} + \cos\frac{\theta_n}{2}\sin\frac{\theta_{n+1}}{2} e^{-i\phi_{n+1}} \,. \tag{3.37}$$

For a non-collinear spin texture, expressed through a static angle $\theta = \theta_{n+1} - \theta_n$ between adjacent sites and $\phi_n = 0$ the matrix element reduce to $\bar{\alpha} = \alpha = \cos\theta/2$ and $\bar{\beta} = \beta = \sin\theta/2$. After expressing the combined Hamiltonian of (3.17) and (3.34) in the Majorana basis and transforming to k-space we find for the Pfaffian

$$\mathrm{Pf}[A(q)] = B_0^2 - [\mu - 2t\alpha\cos(q) + 2\lambda\beta\cos(q)]^2 - [\Delta_0 - 2it\beta\sin(q) - 2i\lambda\sin(q)]^2 \tag{3.38}$$

Here it is not straightforward to derive a simple relation between parameters for the Majorana number. This is due to the additional spin–orbit coupling which intercepts the topological regime of the bare spiral chain. In figure 3.5 we show topological phase diagrams for two sets of parameters.

3.4.4 Numerical Evidence

Previously, we have derived some analytical expressions for the topological

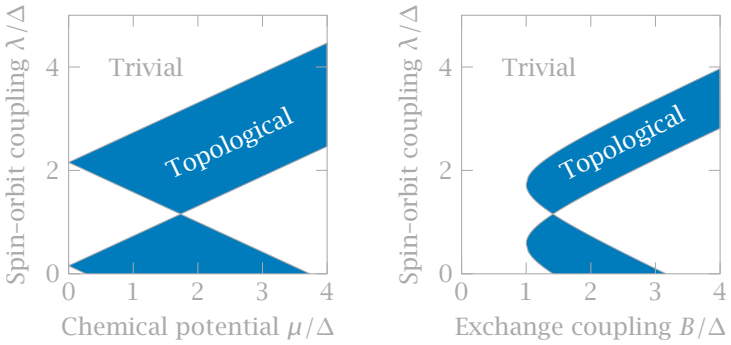

■ *Figure 3.5* Topological phase diagrams from the analytical expression (3.38). The plot on the *left-hand side* shows a phase diagram for constant $B = 2$, the plot on the *right-hand side* one for constant $\mu = 1$. In both cases we have a crossing point of two topological regimes as a result of the interplay between the helical magnet and spin–orbit coupling. Parameters are $t = 2$, $\Delta = 1$, and $\theta = 2\pi/3$.

invariant. The edge states and the corresponding densities of states are not analytically tractable and have to be calculated numerically. This way, we can verify the analytical predictions.

Therefore we compare the nature of the edge states, which emerge in the topological regime for both systems. Figure 3.6 shows the local density of states, resolved over space and energy, for the system (3.12) with 48×1 sites and a helical spin texture without spin–orbit coupling. As in [12], but with a different set of parameters, we find a well-shaped edge state in conjunction with a zero bias peak at the edge of the system. The procedure is also conducted for a system with the same number of sites, but with ferromagnetic order of the impurities and in presence of spin–orbit coupling in figure 3.6. The value of the spin–orbit coupling is determined from the exact analytical matching, determined earlier. In the case of a helical spin texture with a tilting angle of $\theta = 2\pi/3$ between adjacent spins the value of the spin–orbit coupling parameter λ takes the value $\lambda = t \sin(\theta/2) = t \sin(2\pi/6) = \sqrt{3}\, t$. From the two figures we indeed recognise the perfect matching, just as predicted by our calculation.

The chief conclusion which can be drawn from these observations is, that we have gathered further evidence, that the effects of a helical spin-texture can be related to these of spin–orbit coupling. The visual equivalence of the two LDOS strongly suggest that the two systems are related by a unitary transformation.

The question remains whether the topological regime of the system with the helical spin texture is immediately spoiled by spin–orbit coupling. To this end we evaluate our analytical expression for the topological index, which was derived earlier. Additionally we observe the change of the energy spectrum with increasing spin–orbit coupling. The result is shown in figure 3.8.

The figure shows the change of the energy spectrum of (3.12) for a 96×1 chain with open boundary conditions for varying spin–orbit coupling parameter λ. The grey shaded regions are derived from (3.38). The numerical results match the analytical predictions quite well, as we observe a zero bias state in most

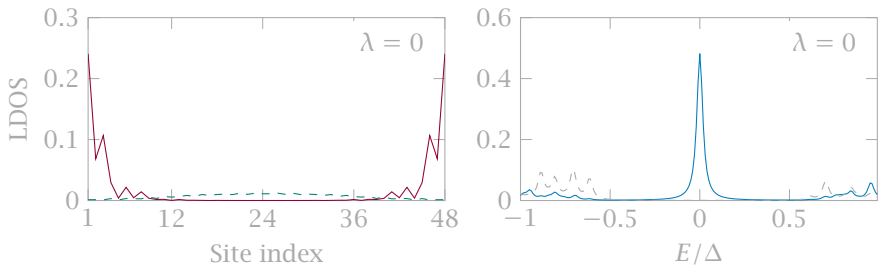

■ *Figure 3.6* The *left-hand side* shows the spatially resolved local density of states of a system with 48×1 sites, a *helical* spin texture, and spin–orbit coupling λ. Shown are the ground state (red) and first excited state (green,dashed). The *right-hand side* shows the local density of states resolved over the energy. Shown are the LDOS at the end of the chain (blue) and in the middle of the chain (grey,dashed). The parameters are $\Delta = 1$, $\mu = 1$, $B = 2$, and $t = 2$. The angle between adjacent spins is chosen as $\theta = 2\pi/3$.

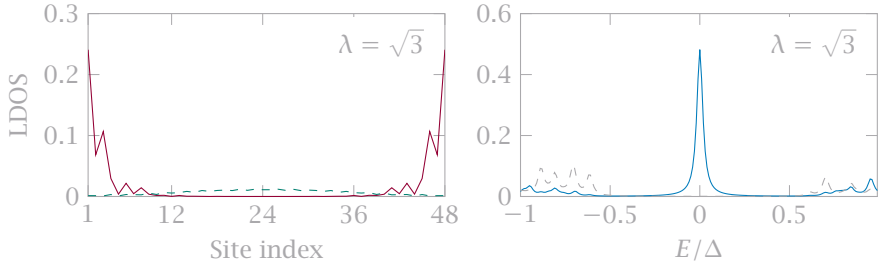

■ *Figure 3.7* The *left-hand side* shows the spatially resolved local density of states of a system with 48×1 sites, a *ferromagnetic* spin texture, and spin–orbit coupling λ. Shown are the ground state (red) and first excited state (green,dashed). The *right-hand side* shows the local density of states resolved over the energy. Shown are the LDOS at the end of the chain (blue) and in the middle of the chain (grey,dashed). The fixed parameters are $\Delta = 1$, $\mu = 1$, $B = 2$, and $t = 1$. The value for λ is chosen according to the exact matching of the two models derived earlier, viz. $\lambda = \sin(2\pi/6) = \sqrt{3}$.

parts of the grey region. The splitting towards the ends of the grey regions is a finite-size effect and can be reduced by choosing longer chains. The 96×1 chain offered the best trade-off between finite-size effects and computation time.

In figure 3.8 there are two topological phases. For increasing λ we start in a topological regime where the red state is located at zero energy. After a gap closing the band structure becomes trivial and the state associated with the red line is shifted back into the bulk. After another gap closing, however, we recover a second topological regime where a different state denoted by a blue line is bound at zero energy.

That is to say, we can close the gap several times and enter and leave topological regimes if the interaction with an external field (here spin–orbit coupling) shifts the states. This result is particularly interesting because there exist two "different" topological regimes in the sense, that the first part is induced by the magnetic coupling whereas the second part is induced by spin–orbit coupling.

These two phases are indeed topologically different because if one introduces a domain wall in the wire where one half of the wire is in the first topological

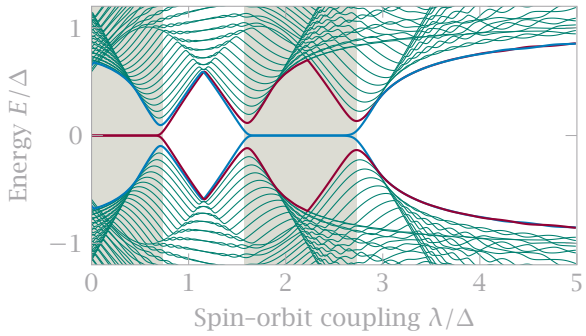

■ *Figure 3.8* The plot shows the change of the energy spectrum of (3.12) for varying spin–orbit coupling parameter λ. The grey shaded regions correspond to the analytically computed topological index W equal to -1. This coincides well with the spectrum, where we observe a zero-bias state in both regions (red/blue). The fixed parameters are $t = 2$, $\mu = 1$, $\Delta = 1$, $B = 2$, and $\theta = 2\pi/3$.

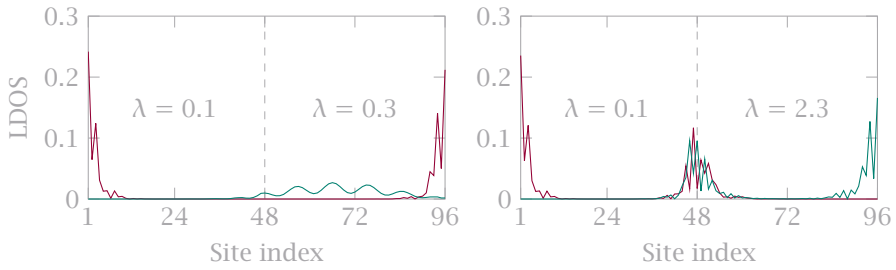

■ *Figure 3.9* We show the local density of states for a system of two connected wires. Plotted are the ground state (red) and first excited state (green). Both wires have different values of λ to introduce a domain wall. On the *left-hand side* both values of λ are from the same topological regime. The resulting LDOS is slightly asymmetric. On the *right-hand side* the two values of λ are from different topological regimes. Clearly, there is a bound state at the domain wall which indicates that the two topological regimes are indeed different. Parameters are $t = 2$, $\mu = 1$, $\Delta = 1$, $B = 2$, and $\theta = 2\pi/3$.

phase and the other half is in the second topological phase one can observe a zero energy bound state at this domain wall, cf. figure 3.9. If they were the same topological phase this bound state at the domain wall would *not* arise. The peculiar interplay of spin–orbit coupling with the magnetic spiral leads to this interesting phase diagram.

To top off the treatment of the one-dimensional wire we investigate the stability of the topological phase under disorder in the spin texture. As previously for the Majorana chain we introduce

$$B_n^\mu \to \begin{cases} B_n^\mu(1+\delta(x_n)) & B^\mu \neq 0 \\ \delta(x_n) & B^\mu = 0 \end{cases} \quad \text{where} \quad \mu \in \{x, y, z\} \tag{3.39}$$

with the uniformly distributed random variable δ in the interval Ω. A different random number is drawn for each component μ of the classical spin. In figure 3.10 we show the sign of the Pfaffian of the Hamiltonian matrix as a function of the disorder strength W where $\delta \in \Omega = [-W, W]$.

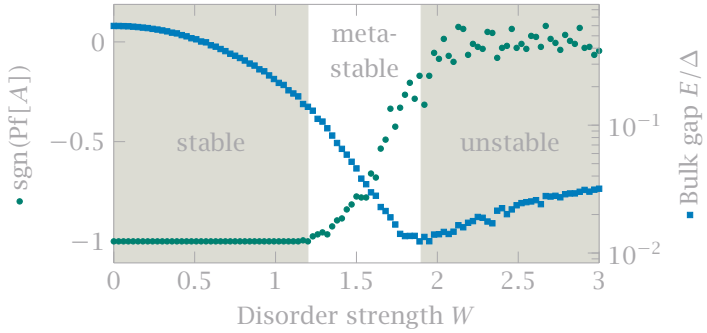

Figure 3.10 We show the sign of the Pfaffian as a function of the disorder strength W. The result is averaged over 400 disorder configurations. Parameters are 96×1 sites, $t = 2$, $\mu = 1$, $\Delta = 1$, $\lambda = 2.3$, $B = 2$, $\theta = 2\pi/3$.

First of all we note that when increasing the disorder strength the sign of the Pfaffian does *not* approach $+1$, i.e. the trivial phase but 0 which indicates a balance between trivial and topological phases. We distinguish three different regimes in the diagram. First, the topologically stable part where the sign of the Pfaffian is always -1. Next we have the topologically meta-stable regime where the bulk gap is non-zero but not all disorder configurations stabilise a topological phase any more. At the transition from the meta-stable to the subsequent unstable part we observe a change of trends in the bulk gap magnitude as it exhibits a turning point. This indicates that, disregarding finite-size effects, the bulk gap had closed in between. The unstable regime is characterised by the fact that now the disorder configuration alone is crucial to whether a topologically stable phase can form and a balance between trivial and topological phase is established.

3.5 Chiral States in a Shiba Lattice

In the previous text we have dealt with the pedagogical model of a one-dimensional chain. Albeit experimentally successful, fabricating atomic chains is very hard in the lab. It has been reported [13,52] that, e.g. Fe tends to form islands on a Pb substrate for non-ideal growth conditions. Therefore we are interested in whether topological phases can emerge in such two-dimensional patches.

3.5.1 Helical Spin Texture

As for the one-dimensional model we begin with a helical spin texture. We stack chains like in figure 3.3 in y-direction with a shift. This texture has

been proposed by Nakosai *et al.* [43] and is depicted in figure 3.11 for better comprehension.

After imposing this spin texture we directly solve the full Hamiltonian (3.4) meaning that we diagonalise the large real space matrix and extract eigenvalues and eigenvectors as in section 2.1.2. To obtain a spectrum of the surface state we impose periodic boundary conditions in x-direction and Fourier transform the extracted eigenvectors along the x-axis. We then plot the modulus squared of the eigenvector for the layer $l = 0$ as a function of the surface momentum versus the corresponding energy eigenvalue, cf. (2.55). The result is shown in figure 3.12.

Because the edge modes are dispersionless bound states their winding number can only take two possible values, zero and one. A similar property has also been observed earlier for the Kitaev chain where we found the Majorana number as an alternative topological invariant. The Majorana number is related to the Pfaffian of the Hamiltonian matrix which is defined according to (2.29). This quantity can be readily calculated from the full real space Hamiltonian and numerically efficient algorithms have been developed [53]. However, the Hamiltonian needs to be expressed in terms of Majorana operators. We have the advantage that our system is particle-hole symmetric and according to [4] the BdG Hamiltonian can be written like

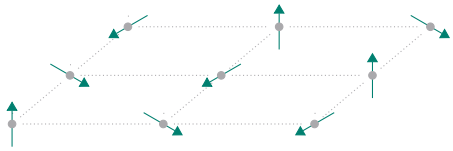

■ *Figure 3.11* Nakosai *et al.* [43] proposed a helical spin texture akin to the one shown for the one-dimensional chain, cf. figure 3.3. The tilt angle between adjacent moments was chosen as $\theta = 2\pi/3$. It is evident from the picture that this texture results in a plane wave along the diagonal of lattice.

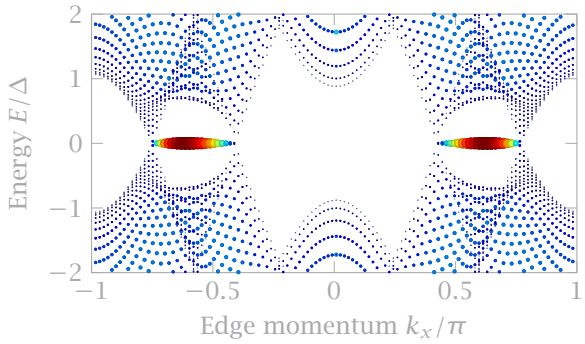

■ *Figure 3.12* Surface density of states for a heterostructure with a helical spin texture as shown in figure 3.11. Dispersionless Majorana modes connect the nodal points. The points are scaled and coloured according to their spectral weight. Parameters are 120×24 sites, $l = 0$, $t = 2$, $\mu = 3$, $\Delta = 1$, $B = 4$, $\theta = 2\pi/3$.

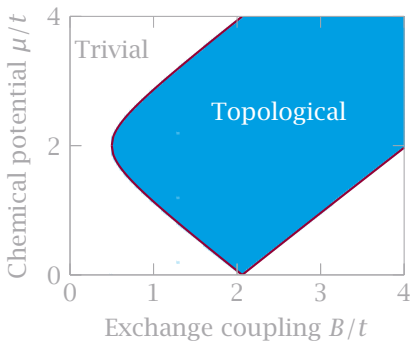

■ *Figure 3.13* Topological phase diagram for the system (3.4) with a helical spin texture. The blue area is the calculated Pfaffian, the red lines indicate the analytical phase boundary. Parameters are $t = 2$, $\Delta = 1$, $\theta_x = \theta_y = 2\pi/3$.

$$H = \begin{bmatrix} \Xi & \Delta \\ -\Delta^* & -\Xi^\top \end{bmatrix} \quad \text{with} \quad \Xi = \Xi^\dagger \,, \quad \Delta = -\Delta^\top \,. \tag{3.40}$$

This can be expressed in the Majorana basis (2.3) in terms of Ξ and Δ, viz.

$$H = \frac{1}{4}\begin{bmatrix} -i(R_- + S_+) & -(R_+ - S_-) \\ (R_+ - S_-) & -i(R_- - S_+) \end{bmatrix} \quad \text{with} \quad R_\pm = \Xi \pm \Xi^\top \,, \quad S_\pm\Delta \pm \Delta^* \,. \tag{3.41}$$

Just as for the one-dimensional chain we can also apply the unitary transformation (3.15). Here we have to apply the transformation twice because the rotation may take place in both x- and y-direction. Ultimately we find

$$\begin{aligned} \mathrm{Pf}[A(\boldsymbol{q})] = B^2 &- [\mu - 2t(\alpha_x \cos(q_x) + \alpha_y \cos(q_y))]^2 \\ &- [\Delta - 2it(\beta_x \sin(q_x) + \beta_y \sin(q_y))]^2 \,, \end{aligned} \tag{3.42}$$

where $\alpha_{x,y} = \cos(\theta_{x,y}/2)$ and $\beta_{x,y} = \sin(\theta_{x,y}/2)$. To resemble a spin texture as in figure 3.11 we have to set $\theta_x = \theta_y$.

Now we can derive analytical as well as numerical expressions for the Majorana number. We have plotted both in figure 3.13. Clearly, the results match very well and the surface density of states in figure 3.12 shows gapless surface states for a parameter set from the topological region, further supporting these conclusions.

3.5.2 Ferromagnetic Spin Texture with Spin–Orbit Coupling

A ferromagnetic spin texture is where all classical spins are aligned in the same direction. For the simplicity of the calculation we choose the z-direction. To engineer topological phases we need to employ an additional Rashba-type spin–orbit coupling. The corresponding operator was derived earlier and the full Hamiltonian is given by (3.12). This model is diagonal in k-space and can be

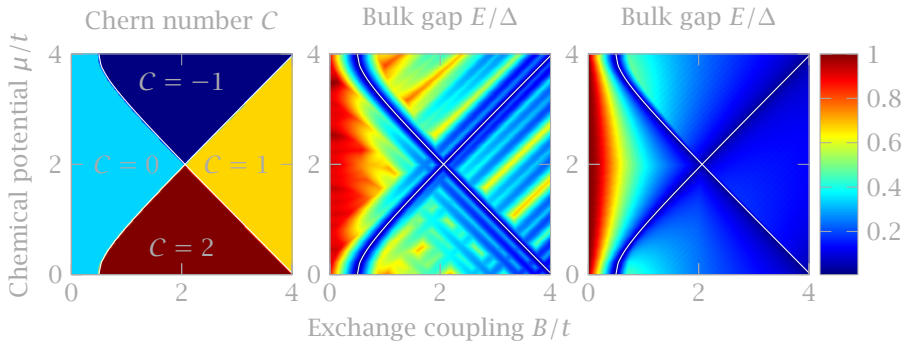

■ *Figure 3.14* Topological phase diagram for the Shiba lattice in combination with strong spin–orbit coupling. On the *left* we show the Chern numbers of the different phases, in the *middle* we show the excitation gap as computed in the real space model, and on the *right* we show the excitation gap computed analytically. The white lines are the analytically determined phase boundaries. Parameters are 12×12 sites, $t = 2$, $\Delta = 1$, $\lambda = 1$.

readily obtained by straightforward Fourier transformation. In Nambu grading with the spinor $\Psi_{\boldsymbol{k}} = (c_{\boldsymbol{k},\uparrow}, c_{\boldsymbol{k},\downarrow}, c^\dagger_{-\boldsymbol{k},\uparrow}, c^\dagger_{-\boldsymbol{k},\downarrow})^\top$ one has

$$H = \sum_{\boldsymbol{k}} \Psi^\dagger_{\boldsymbol{k}} \begin{bmatrix} \xi_{\boldsymbol{k}}\sigma_0 + \boldsymbol{B}\cdot\boldsymbol{\sigma} + \boldsymbol{l}_{\boldsymbol{k}}\cdot\boldsymbol{\sigma} & \Delta i\sigma_y \\ \Delta(i\sigma_y)^\dagger & -(\xi_{\boldsymbol{k}}\sigma_0 + \boldsymbol{B}\cdot\boldsymbol{\sigma} + \boldsymbol{l}_{\boldsymbol{k}}\cdot\boldsymbol{\sigma})^\top \end{bmatrix} \Psi_{\boldsymbol{k}} \,, \tag{3.43}$$

with $\boldsymbol{l}_{\boldsymbol{k}} = \lambda(\sin k_y, -\sin k_x, 0)^\top$ and $\xi_{\boldsymbol{k}} = 2t(\cos k_x + \cos k_y) - \mu$. The eigenvalues can be determined analytically but the resulting expressions are very lengthy and we omit them here for the sake of brevity. However, we will use the analytical expression later to obtain the excitation gap.

In contrast to the helical spin texture where we had found Majorana bound states connecting the nodal points in the gap we find a fully gapped bulk and chiral edge states for this configuration. This means that we can compute some quantities which were not considered before, viz. the Chern number and the expectation value of the current operator.

Depending on the chemical potential and exchange coupling we find four distinct topological phases with Chern numbers

$$C = -1, 0, 1, 2$$

respectively. These phases are separated by gapless lines in the excitation spectrum which can be computed from the real space model (3.12) or from the energy eigenvalues of its k-space diagonal counterpart (3.43). We show the resulting topological phase diagram in figure 3.14. We see that the excitation gap diagram obtained from the real space calculation is haunted by finite-size effects for lattices as small as 12×12 sites though the gapless lines are resolved nicely.

Now it is interesting to look at the surface states associated with the different phases. We pick a certain parameter set and calculate the surface density of

states (2.55). The resulting graph is plotted in figure 3.15. Obviously the bulk is fully gapped while the edge state crosses through it.

Similar to the chiral p-wave superconductor we can compute the current operator for (3.12). Again we only present the result for each vector component.

$$\begin{aligned} j_x &= it \sum_{n,\sigma} (f^\dagger_{n,\sigma} f_{n+x,\sigma} - f^\dagger_{n+x,\sigma} f_{n,\sigma}) \\ &\quad + i\lambda \sum_n (f^\dagger_{n,\downarrow} f_{n+x,\uparrow} + f^\dagger_{n+x,\downarrow} f_{n,\uparrow} - f^\dagger_{n+x,\uparrow} f_{n,\downarrow} - f^\dagger_{n,\uparrow} f_{n+x,\downarrow}) \,, \quad (3.44) \\ j_y &= it \sum_{n,\sigma} (f^\dagger_{n,\sigma} f_{n+y,\sigma} - f^\dagger_{n+y,\sigma} f_{n,\sigma}) \\ &\quad - \lambda \sum_n (f^\dagger_{n,\downarrow} f_{n+y,\uparrow} + f^\dagger_{n+y,\downarrow} f_{n,\uparrow} + f^\dagger_{n+y,\uparrow} f_{n,\downarrow} + f^\dagger_{n,\uparrow} f_{n+y,\downarrow}) \,. \quad (3.45) \end{aligned}$$

To obtain a layer resolved current operator, we Fourier transform the two components along their respective direction. That is to say, we Fourier transform j_x along x and j_y along y. We adopt the indices i, j to correspond to x, y-layers. Thus, to extract the current in a single layer, we simply look at the i-th (j-th) term of the following expression.

$$\begin{aligned} j_x &= -2t \sum_{k_x,j,\sigma} \sin k_x \, f^\dagger_{k_x,j,\sigma} f_{k_x,j,\sigma} \\ &\quad - 2\lambda \sum_{k_x,j} \cos k_x (-i f^\dagger_{k_x,j,\downarrow} f_{k_x,j,\uparrow} + i f^\dagger_{k_x,j,\uparrow} f_{k_x,j,\downarrow}) \,, \quad (3.46) \\ j_y &= -2t \sum_{i,k_y,\sigma} \sin k_y \, f^\dagger_{i,k_y,\sigma} f_{i,k_y,\sigma} \\ &\quad - 2\lambda \sum_{i,k_y} \cos k_y (f^\dagger_{i,k_y,\downarrow} f_{i,k_y,\uparrow} + f^\dagger_{i,k_y,\uparrow} f_{i,k_y,\downarrow}) \,. \quad (3.47) \end{aligned}$$

The current operator itself is not an interesting quantity, but its expectation value is, because this is a measurable quantity. Therefore, to obtain the current in a layer we compute the expectation values

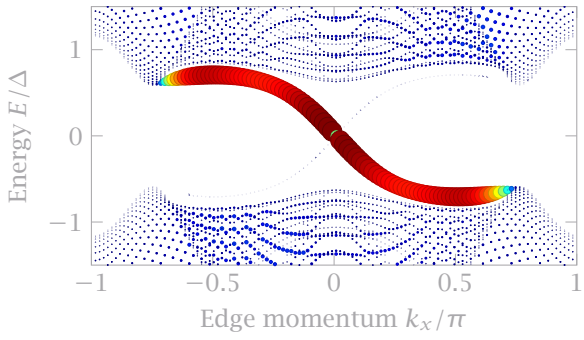

■ *Figure 3.15* Surface density of states for a heterostructure with a ferromagnetic spin texture and Rashba type spin–orbit coupling. A chiral edge state with Chern number $C = -1$ crosses through the full gap. The points are scaled and coloured according to their spectral weight. Parameters are 120×24 sites, $l = 0$, $t = 1$, $\mu = 3$, $\Delta = 1$, $\lambda = 1$, $B = 2$.

$$\langle j_x^j(k_x)\rangle = \sum_\lambda \langle \psi^\lambda_{k_x,j}|j_x|\psi^\lambda_{k_x,j}\rangle \quad \text{and} \quad \langle j_y^i(k_y)\rangle = \sum_\lambda \langle \psi^\lambda_{i,k_y}|j_y|\psi^\lambda_{i,k_y}\rangle \tag{3.48}$$

where the sums run over the eigenstate number λ, i.e. $|\psi^\lambda\rangle$ is the eigenstate of H with energy eigenvalue E_λ.

As in section 2.2.4 we compute the expectation value of the current density operator for the state shown in figure 3.15. In figure 3.16 we show the real space current with vectors and the symmetrised k-space current on the surface at $l = 0$. The vectors indicate a current going around the edges of the patch. The magnitude is colour coded where red means stronger. The signal in the edge momentum resolved current is similar to the one found for the chiral p-wave superconductor.

Next we investigate the stability of the topological phase under disorder in the spin texture. Akin to Kitaev's chain we introduce the site dependent magnetic moments

$$B_n^\mu = \begin{cases} B^\mu(1+\delta(x_n)) & B^\mu \neq 0 \\ \delta(x_n) & B^\mu = 0 \end{cases} \quad \text{where} \quad \mu \in \{x, y, z\}\,, \tag{3.49}$$

with the uniformly distributed random variable δ in the interval Ω. A different random number is drawn for each component μ of the classical spin. In figure 3.17 we show the Chern number as a function of the disorder strength W where $\delta \in \Omega = [-W, W]$. The topological phase is almost perfectly stable up to $W = 1$ which corresponds to a disorder strength of 100%.

3.5.3 Helical Spin Texture with Spin–Orbit Coupling

Just as for the one-dimensional system we carry on to a helical spin texture in combination with strong spin–orbit coupling. Because the spin–orbit interaction term does not commute with the unitary transformation (3.15) we cannot perform an analytical treatment of this system.

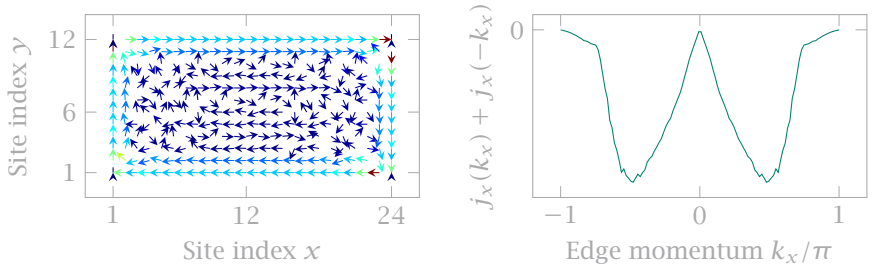

■ *Figure 3.16* We show the expectation value of the current operator for a state with Chern number $C = -1$. On the *left-hand side* we plot the current density in real space with vectors for 24×12 sites with open boundary conditions. One can clearly see the current going around the system. On the *right-hand side* we plot the symmetrised current of the layer $l = 0$ for 120×24 sites with periodic boundary conditions along the edge. Parameters are $t = 1$, $\mu = 3$, $\Delta = 1$, $\lambda = 1$, $B = 2$.

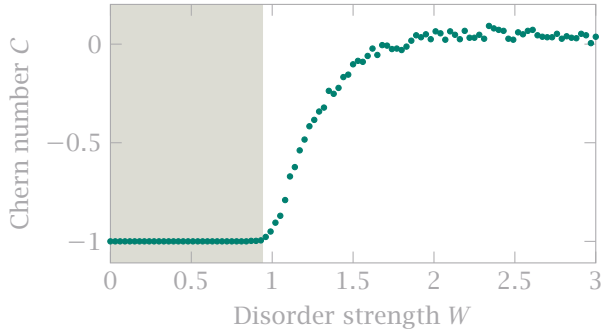

■ *Figure 3.17* We show the Chern number C as a function of the disorder strength W for the state shown in figure 3.15. The result is averaged over 400 disorder configurations. Parameters are 12×12 sites, $t = 1$, $\mu = 3$, $\Delta = 1$, $\lambda = 1$, $B = 2$.

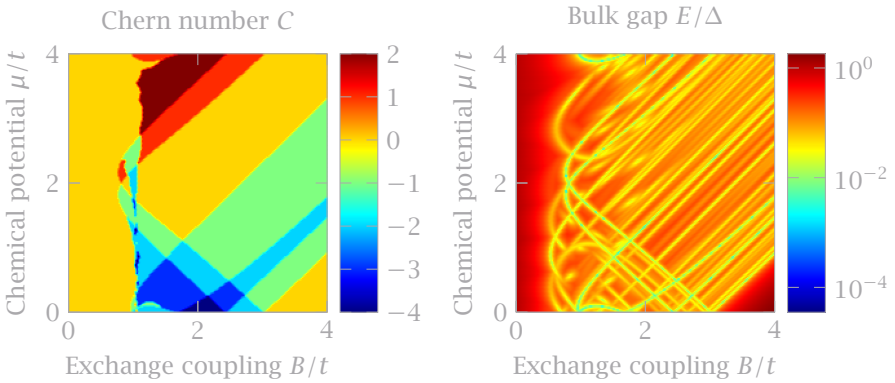

■ *Figure 3.18* Topological phase diagram for a helical spin texture in combination with strong spin–orbit coupling. On the *left* we show the Chern numbers of the different phases, on the *right* we show the associated excitation gap in log scale. The log scale accounts for the overall gap being quite small. Parameters are 24×24 sites, $t = 2$, $\Delta = 1$, $\lambda = 1$, $\theta_x = \theta_y = 2\pi/3$.

However, as presented in appendix A.1 we can compute the Chern number from real space calculations. In figure 3.18 we show a topological phase diagram for a system of 12×12 sites and a helical spin texture as shown in figure 3.11. Actually, this diagram is an extension of figure 3.13 for non-zero spin–orbit coupling λ. We find many different phases with sometimes high Chern number. Unfortunately, as for the case of a ferromagnetic texture presented in figure 3.14, the results suffer from finite-size effects now leading to probably ill-predicted topological phases. This is evident from changes of the Chern number without apparent bulk gap closing. For example in the area around $(B/t, \mu/t) = (1, 3.5)$ we observe a change from $C = 0$ to $C = 2$ without a gap closing at the sharp phase boundary.

Because the overall bulk gap is very small in comparison to the superconducting gap we pick a point in a topologically non-trivial regime with large gap for closer inspection of the associated surface state. For a state with Chern number

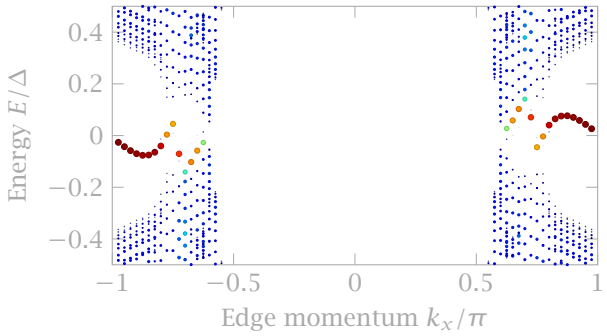

■ *Figure 3.19* Surface density of states for a heterostructure with a helical spin texture and strong spin–orbit coupling. The bulk gap is very small and it is hard to interpret the surface state. The points are scaled and coloured according to their spectral weight. Parameters are 81×81 sites, $l = [0, 9]$, $t = 2$, $\mu = 3$, $\Delta = 1$, $\lambda = 1$, $B = 6$, $\theta_x = \theta_y = 2\pi/3$.

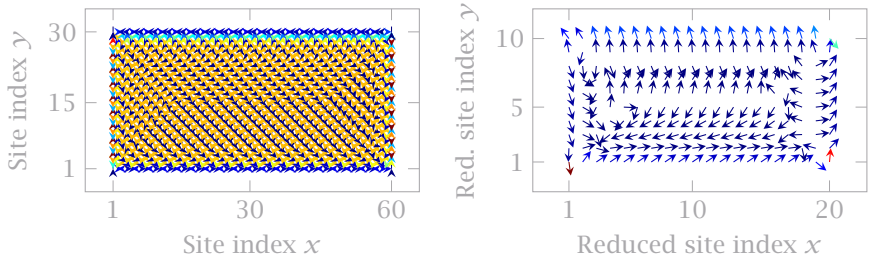

■ *Figure 3.20* We show the expectation value of the current operator for a state with Chern number $C = -1$. On the *left-hand side* we plot the current density in real space with vectors for 60×30 sites with open boundary conditions. On the *right-hand side* we plot the same current but averaged over the 3×3 unit cell. Parameters are $t = 2$, $\mu = 3$, $\Delta = 1$, $\lambda = 1$, $B = 6$, $\theta_x = \theta_y = 2\pi/3$.

$C = -1$ and associated bulk gap of $E/\Delta \approx 0.1$ we show the surface density of states (SDOS) in figure 3.19. It seems as if the state breaks the time-reversal symmetry but the full bulk gap is not clearly visible.

Next we compute the expectation value of the current operator for this state. The result is shown in figure 3.20. Unfortunately, the arrows have seemingly random orientations and no clear direction of the current is evident. In an attempt to remedy this we average the current of the 3×3 unit cell but to no avail. Now there are components in the current pointing out of the system which is physically impossible.

We can conclude that stable topological phases probably exist in a system with helical magnetic order and strong spin–orbit coupling. Unfortunately, the bulk gap is small which makes it hard to determine the exact phase boundaries. The surface states seem to have chiral character although it is questionable whether there is a full gap present in figure 3.19. The expectation value of the current operator does not look very promising as well.

The question remains what is the origin of these uncertainties. For the phase

diagram in figure 3.18 we can conclude that there is are similar finite-size effects as for the ferromagnetic texture where we observed a strong influence of finite size in comparison with an analytical solution. One has to keep in mind that for the helical spin texture a system of 24×24 sites corresponds to only 8×8 unit cells. This could possibly be resolved by taking a larger lattice. However, the computation of the Chern number is very costly and such a calculation probably takes up several weeks, if not months.

These finite-size effects could also explain the weird behaviour of the surface state and the current operator. Perhaps the actual bulk gap is much smaller at the point we selected or the system is not even in a topological phase due to a wrong prediction of the Chern number.

In any case, the problem remains unsolved.

Summary of Chapter 3

Magnetic impurities in a superconductor give rise to sub-gap bound states. The band structure of these states can exhibit topologically non-trivial behaviour depending on the alignment of the classical spins. This can be exploited to engineer an effective p-wave pairing in a conventional superconductor [11–14, 36].

Among others, Nadj-Perge *et al.* [12] showed that a planar spiral configuration of magnetic adatoms supports Majorana edge modes at the ends of a one-dimensional chain. In section 3.4.1 we reproduced some of these results as a pedagogical introduction. Based on this we show in section 3.4.2 that the effects of the helical spin texture can be related *exactly* to those of spin–orbit coupling in the host superconductor with a ferromagnetic alignment of the impurity spins by unitary transformation. Since recent studies [49,50] suggest that a ferromagnetic spin texture is not stable in the superconducting phase, we study the interplay of a helical spin texture with intrinsic Rashba-type spin–orbit coupling along the chain in section 3.4.3. We derive an analytical expression for the topological invariant (3.38) and show that topological phases exist even for strong spin–orbit interaction. The corresponding topological phase diagram is shown in figure 3.5. Using real space tight-binding calculations we conclude that two distinct topological regimes form even though they possess the same value of the topological invariant. Even for strong spin–orbit interaction the topological phase is robust against random static disorder in the spin texture.

One-dimensional chains of magnetic adatoms are hard to fabricate in the lab and it has been reported [13, 52] that, e.g. Fe tends to form island on a Pb substrate. In section 3.5.1 we study a two-dimensional helical spin texture originally proposed in [43], visualised in figure 3.11. The surface density of states in figure 3.12 indicates dispersionless Majorana bound states at the edges and we

conclude that the topological invariant has $\mathbb{Z}_2$ character. Again, we can calculate the Pfaffian analytically and construct a topological phase diagram, cf. figure 3.13, where we compare analytical and numerical results. In section 3.5.2 we study a ferromagnetic spin texture with spin–orbit coupling. The spin–orbit coupling gives rise to an interesting phase diagram with several distinct topological phases. We obtain the Chern number from tight-binding calculations using the algorithms outlined in appendix A.1 and show it alongside the excitation gap in figure 3.14. Non-zero winding numbers indicate a spontaneous current going around the edges of the system. The expectation value of the current operator is shown in figure 3.16. The topological phase is robust against random static disorder in the ferromagnetic spin texture. Finally, in section 3.5.1 we study the helical spin texture from figure 3.11 in conjunction with Rashba-type spin–orbit coupling and find a rich phase diagram, cf. figure 3.18. Finite-size effects make it hard to verify the validity of the results. The surface density of states in figure 3.19 and the spontaneous edge current in figure 3.20 are hard to interpret. Extended discussions can be found in the corresponding section.

Appendix A

Algorithms

A.1 Chern Number

The Chern number can be defined for quantum states with at least two parameters such as the Brillouin zone in two dimensions. Usually the Chern number is defined as

$$C = \frac{1}{2\pi i} \sum_{\text{filled bands}} \int_{\text{BZ}} \mathrm{d}\boldsymbol{k}\, \mathcal{F}_{12}(\boldsymbol{k}) \tag{A.1}$$

where $\mathcal{F}_{12}(\boldsymbol{k})$ is the Berry curvature which is defined in terms of the Berry connection $\mathcal{A}_\mu(\boldsymbol{k})$

$$\mathcal{F}_{12}(\boldsymbol{k}) = \frac{\partial}{\partial k_x}\mathcal{A}_y(\boldsymbol{k}) - \frac{\partial}{\partial k_y}\mathcal{A}_x(\boldsymbol{k}) \quad \text{with} \quad \mathcal{A}_\mu(\boldsymbol{k}) = \langle n(\boldsymbol{k})|\frac{\partial}{\partial k_\mu}|n(\boldsymbol{k})\rangle \tag{A.2}$$

with the normalised Bloch wave functions $|n(k)\rangle$.

In numerical calculations the Hamiltonian is diagonalised at discrete points in the Brillouin zone and the above formula becomes impractical because numerical derivatives and integrals can only be evaluated with good precision for many lattice points and high order of expansion.

Fukui *et al.* [54] devised an efficient algorithm to evaluate the Chern number in a discretised Brillouin zone. The discrete momenta in the Brillouin zone are given by $\boldsymbol{k}_n = (k_n^x, k_n^y)$. Define the U(1) link variable from the wave functions of the n-th band as

$$U_\mu(\boldsymbol{k}_n) = \frac{\langle n(\boldsymbol{k})|n(\boldsymbol{k}+\hat{\mu})\rangle}{|\langle n(\boldsymbol{k})|n(\boldsymbol{k}+\hat{\mu})\rangle|} \tag{A.3}$$

where $\hat{\mu}$ is the lattice displacement vector in μ-direction. From the link variable define the discretised Berry curvature

$$F_{12}(\boldsymbol{k}_n) = \ln\left(\frac{U_x(\boldsymbol{k}_n)U_y(\boldsymbol{k}_n+\hat{x})}{U_x(\boldsymbol{k}_n+\hat{y})U_y(\boldsymbol{k}_n)}\right) \quad \text{such that} \quad -\pi < \frac{1}{i}F_{12}(\boldsymbol{k}_n) \leq \pi\,. \tag{A.4}$$

To fulfil this condition we always have to choose the first branch of the complex logarithm. With this the Chern number is defined as

$$C = \frac{1}{2\pi i} \sum_{\text{filled bands}} \sum_{n} F_{12}(\boldsymbol{k}_n) \,. \tag{A.5}$$

But what if we cannot diagonalise the Hamiltonian in k-space? This is the case for an arbitrary spin texture. A real space approach to compute the Chern number is needed. Zhang *et al.* [55] devised an algorithm were only a single exact diagonalization of the Hamiltonian is needed, in contrast to [54] were the Hamiltonian has to be diagonalised for each lattice point in k-space.

Consider a two-dimensional lattice of size $N = L_x \times L_y$ and define twisted boundary conditions such that

$$\varphi^m_\theta(x + L_x, y) = e^{i\theta_x}\varphi^m_\theta(x, y) \quad \text{and} \quad \varphi^m_\theta(x, y + L_y) = e^{i\theta_y}\varphi^m_\theta(x, y) \,. \tag{A.6}$$

For twisted boundary conditions the Chern number is given by

$$C = \frac{1}{2\pi i} \int_{\mathbb{T}_\theta} \mathrm{d}\theta \langle \nabla_\theta \Psi_\theta | \times | \nabla_\theta \Psi_\theta \rangle \tag{A.7}$$

with $\theta = (\theta_x, \theta_y)$. The state Ψ_θ denotes the many-body wave function which is given in terms of a Slater determinant of the single particle wave functions φ^m_θ where $m = 1, \ldots, M$ denotes all the *occupied* states.

As a next step the single particle wave functions are Fourier transformed and one has

$$\varphi^m_\theta(\boldsymbol{r}) = \frac{1}{\sqrt{N}} \sum_{\boldsymbol{k}} e^{i\boldsymbol{k}\cdot\boldsymbol{r}} \Phi^m(\boldsymbol{k}) \,. \tag{A.8}$$

The twisted boundary conditions are contained in $\boldsymbol{k}$ which can be decomposed such that $\boldsymbol{k} = \boldsymbol{k}^0 + \boldsymbol{q}$ with

$$\boldsymbol{k}^0 = \left(\frac{2\pi x}{L_x}, \frac{2\pi y}{L_y} \right) \quad \text{and} \quad \boldsymbol{q} = \left(\frac{\theta_x}{L_x}, \frac{\theta_y}{L_y} \right) . \tag{A.9}$$

This is very convenient because $\boldsymbol{k}^0$ are the momenta for conventional periodic boundary conditions. We perform a change of variables in (A.7) from θ to $\boldsymbol{q}$. This changes the integration domain $\mathbb{T}_\theta \to R_{\boldsymbol{q}} = [0, 2\pi/L_x) \times [0, 2\pi/L_y)$.

$$C = \frac{1}{2\pi i} \int_{R_{\boldsymbol{q}}} \mathrm{d}\boldsymbol{q} \langle \nabla_{\boldsymbol{q}} \Psi_{\boldsymbol{q}} | \times | \nabla_{\boldsymbol{q}} \Psi_{\boldsymbol{q}} \rangle \tag{A.10}$$

which is according to Stokes' theorem

$$C = \frac{1}{2\pi i} \oint_{\partial R_{\boldsymbol{q}}} \mathrm{d}\boldsymbol{l}_{\boldsymbol{q}} \langle \Psi_{\boldsymbol{q}} | \nabla_{\boldsymbol{q}} \Psi_{\boldsymbol{q}} \rangle \tag{A.11}$$

where $\partial R_{\boldsymbol{q}}$ denotes the boundary around the rectangle $R_{\boldsymbol{q}}$. This boundary is discretised into segments $\boldsymbol{q}_\alpha$. The derivatives are replaced by discrete differences and the integral is turned into a sum. Then the Chern number is given by

$$C = \frac{1}{2\pi} \sum_{\alpha} \arg[\det(C_{\alpha,\alpha+1})] \tag{A.12}$$

where $\arg(\cdot)$ is the angle of a complex number and $C_{\alpha,\alpha+1}$ are $M \times M$ coupling matrices. The matrix elements are given by

$$C^{mn}_{\alpha,\alpha+1} = \langle \Phi^m(\boldsymbol{k}^0 + \boldsymbol{q}_\alpha) | \Phi^n(\boldsymbol{k}^0 + \boldsymbol{q}_{\alpha+1}) \rangle \, . \tag{A.13}$$

It is also possible to compute the product of all coupling matrices $C_{\alpha,\alpha+1}$ first and then diagonalise the resulting matrix. The sum of the angle of the eigenvalues is again proportional to the Chern number. For sufficiently large systems, i.e. $L_x, L_y \gg 1$ it suffices to evaluate the coupling matrices for four distinct points q_α

$$q_0 = (0,0) \, , \quad q_2 = \left(\frac{2\pi}{L_x}, 0\right) , \quad q_3 = \left(0, \frac{2\pi}{L_y}\right) , \quad q_4 = \left(\frac{2\pi}{L_x}, \frac{2\pi}{L_y}\right) . \tag{A.14}$$

Using the inverse Fourier transformation of (A.13) we obtain the real space expression

$$C^{mn}_{\alpha,\alpha+1} = \langle \varphi^m_{\theta=0} | e^{i(\boldsymbol{q}_\alpha - \boldsymbol{q}_{\alpha+1})\boldsymbol{r}} | \varphi^n_{\theta=0} \rangle \, . \tag{A.15}$$

We diagonalise the product $\tilde{C} = C_{0,1} C_{1,2} C_{2,3} C_{3,0}$ of the coupling matrices to obtain its eigenvalues λ_m and the Chern number

$$C = \frac{1}{2\pi} \sum_{m} \arg(\lambda_m) \, . \tag{A.16}$$

To conclude, we test both algorithms against the chiral p-wave superconductor (2.38) using the BdG form (2.39) to apply the algorithm by Fukui *et al.* [54]. The results are shown alongside the analytical solution in figure A.1.

Both algorithms show very good agreement with the analytical solution,

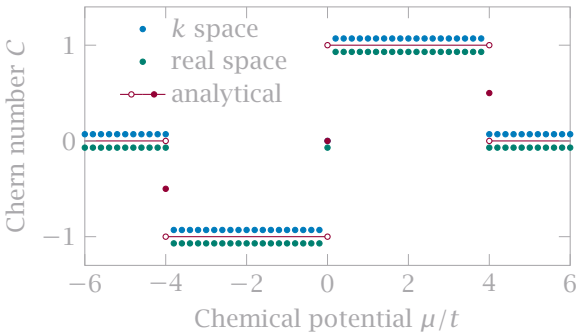

■ *Figure A.1* We compare the two different algorithms for the computation of the Chern number on a discrete lattice with the analytical solution of (2.42). Discontinuous points are shown as unfilled dots. For better visibility the points were shifted off their integer values. Both methods show very good agreement for even small lattice sizes. Parameters are 11×11 sites, $t = 1$, $\Delta = 1$.

which is remarkable considering the small lattices used in the picture. The only difficulties arise at the points where the bulk gap closes, i.e. $\mu = 0, \pm 4t$. For $\mu = \pm 4t$ both algorithms converge to zero rather than the exact one half. At $\mu = 0$, however, the k-space algorithm does not converge due to diverging Berry curvature at two points in the Brillouin zone. This is not really an issue because at these points the Chern number is not well defined anyway and the fact that the analytical solution yields nice values is a pure coincidence.

Summary

English Summary

The main topic of this work was to investigate whether an artificial heterostructure between a conventional *s*-wave superconductor with strong spin–orbit coupling and a non-collinear magnet can host topological phases.

For topological phases to emerge the gap function has to have odd parity. This is the case for a *p*-wave superconductor. In chapter 2 we study two model systems with *p*-wave superconductivity to gain some intuition and to introduce tools needed later. Kitaev [9] showed that a one-dimensional chain can host unpaired Majorana modes at its ends. Because of their non-local character these modes are robust against disorder and are therefore promising candidates for building blocks in a quantum storage. Kitaev's chain can be promoted to two dimensions, where we find helical Majorana modes which propagate around the edges of the system. Majorana bound states at vortices in the superconductor exhibit non-Abelian braiding statistics and could thus be used to implement quantum gates.

Intrinsic *p*-wave superconductors are rare in nature. It is thus desirable to engineer an *effective p*-wave pairing where electrons of the same spin are paired together in contrast to conventional superconductors, which pair electrons of opposite spin. To introduce *p*-wave pairing magnetic impurities are introduced into the conventional superconductor. Bound states form at these impurities and depending on the alignment of the classical impurity spins their band structure can exhibit non-trivial topology [11–15,36].

In chapter 3 we study one- and two-dimensional systems of magnetic adatoms on a conventional *s*-wave superconductor with and without intrinsic spin–orbit coupling. In a one-dimensional wire we show that the effects of a helical magnetic order can be related *exactly* to those of Rashba-type spin–orbit coupling along the wire and ferromagnetic ordering of the impurity spins. We then study the interplay of the helical spin texture with string spin–orbit coupling and find an interesting phase diagram. By numerical simulation we verify our analytical results and show that the topological phase is robust against random static disorder.

For a two-dimensional *s*-wave superconductor and helical spin texture there exist Majorana bound states at the edges. The topological phase diagram for the relevant $\mathbb{Z}_2$ invariant can be calculated analytically. Imposing ferromagnetic order and spin–orbit coupling gives rise to a richer phase diagram with several distinct topological phases. Their non-zero Chern number indicates the presence of a spontaneous current around the edges which was extracted

from numerical calculations. These phases are also robust against random static disorder in the spin texture. The interplay of the helical spin texture and spin–orbit coupling exhibits a rich phase diagram with sometimes high Chern number.

Deutsche Zusammenfassung

Das Hauptthema dieser Arbeit war die Frage, ob eine künstliche Heterostruktur zwischen einem konventionellen *s*-Wellen-Supraleiter mit starker Spin-Bahn-Kopplung und einem nicht kollinearen Magnet topologische Phasen besitzt.

Damit topologische Phasen auftreten können muss die Energielücke ungerade Parität haben. Dies ist der Fall für einen *p*-Wellen-Supraleiter. In Kapitel 2 studieren wir zwei Modellsysteme mit *p*-Wellen-Supraleitung um etwas Intuition zu erhalten und die später benötigten Werkzeuge kennen zu lernen. Kitaev [9] zeigte, dass eindimensionale Ketten ungepaarte Majoranamoden an den Enden aufweisen können. Aufgrund ihres nichtlokalen Charakters sind diese Moden robust gegenüber Unordnung und deshalb vielversprechende Kandidaten für Bausteine in einem Quantenspeicher. Die Kitaev-Kette kann auf zwei Dimensionen erweitert werden, wo wir helikale Majoranamoden finden, welche entlang der Ränder des Systems propagieren. Gebundene Majoranazustände in den Vortizes eines Supraleiters weisen nicht-Abelsche Vertauschungsstatistik auf und sind deshalb zur Realisierung von Quantengattern geeignet.

Intrinsische *p*-Wellen-Supraleiter kommen in der Natur selten vor. Es ist daher wünschenswert *effektive p*-Wellen-Supraleitung zu erzeugen, sodass Elektronen des gleichen Spins gepaart werden, im Gegensatz zu konventionellen Supraleitern, welche Elektronen mit verschiedenem Spin paaren. Um diese Entartung aufzuheben bringt man magnetische Verunreinigungen in den konventionellen Supraleiter ein. An diesen Verunreinigungen bilden sich gebundene Zustände, deren Bandstruktur abhängig von der Ausrichtung der klassischen Spins nicht-triviale Topologie aufzeigt [11–15,36].

In Kapitel 3 untersuchen wir ein- und zweidimensionale Systeme mit magnetischen Adatomen auf einem konventionellen *s*-Wellen-Supraleiter mit und ohne intrinsischer Spin-Bahn-Kopplung. An einer eindimensionalen Kette zeigen wir, dass die Auswirkungen einer helikalen magnetischen Ordnung deren von Rasbaartiger Spin-Bahn-Kopplung und ferromagnetischer Ordnung der klassischen Spins *exakt* entsprechen. Wir untersuchen außerdem das Wechselspiel der helikalen Spintextur mit starker Spin-Bahn-Kopplung und finden ein interessantes Phasendiagramm. Wir belegen unsere analytischen Resultate mit numerischen Simulationen und zeigen, dass die topologische Phase robust gegen zufällige statische Unordnung ist.

Bei einem zweidimensionalen *s*-Wellen-Supraleiter mit helikaler Spintextur existieren gebundene Majoranazustände and den Rändern. Das topologische Phasendiagramm der zugehörigen $\mathbb{Z}_2$-Invarianten kann analytisch berechnet

werden. Ferromagnetische Ordnung und Spin-Bahn-Kopplung führen zu einem vielfältigeren Phasesdiagramm mit mehreren unterschiedlichen topologischen Phasen. Deren nichtverschwindende Chernzahl weist auf einen spontanen Strom um den Rand herum hin, welcher numerisch berechnet wurde. Diese Phasen sind ebenso robust gegenüber zufälliger statischer Unordnung in der Spintextur. Das Wechselspiel der helikalen Spintextur mit Spin-Bahn-Kopplung führt zu einem vielfältigen Phasendiagram mit manchmal hoher Chernzahl.

Ehrenwörtliche Erklärung

Ich erkläre,

- dass ich diese Masterarbeit selbständig verfasst habe,
- dass ich keine anderen als die angegebenen Quellen benutzt und alle wörtlich oder sinngemäß aus anderen Werken übernommenen Aussagen als solche gekennzeichnet habe,
- dass die eingereichte Arbeit weder vollständig noch in wesentlichen Teilen Gegenstand eines anderen Prüfungsverfahrens gewesen ist,
- dass ich die Arbeit weder vollständig noch in Teilen bereits veröffentlicht habe, es sei denn, der Prüfungsausschuss hat die Veröffentlichung vorher genehmigt
- und dass der Inhalt des elektronischen Exemplars mit dem des Druckexemplars übereinstimmt.

Stuttgart, 19. Oktober 2016 *Henri Menke*

References

[1] M. König, S. Wiedmann, C. Brüne, A. Roth, H. Buhmann, L.W. Molenkamp, X.-L. Qi, and S.-C. Zhang, „Quantum Spin Hall Insulator State in HgTe Quantum Wells“, Science **318**, 766–770 (2007).

[2] K. v. Klitzing, G. Dorda, and M. Pepper, „New Method for High-Accuracy Determination of the Fine-Structure Constant Based on Quantized Hall Resistance“, Phys. Rev. Lett. **45**, 494–497 (1980).

[3] D.J. Thouless, M. Kohmoto, M.P. Nightingale, and M. den Nijs, „Quantized Hall Conductance in a Two-Dimensional Periodic Potential“, Phys. Rev. Lett. **49**, 405–408 (1982).

[4] C.-K. Chiu, J.C.Y. Teo, A.P. Schnyder, and S. Ryu, „Classification of topological quantum matter with symmetries“, Rev. Mod. Phys. **88**, 035005 (2016).

[5] A.P. Schnyder, S. Ryu, A. Furusaki, and A.W.W. Ludwig, „Classification of topological insulators and superconductors in three spatial dimensions“, Phys. Rev. B **78**, 195125 (2008).

[6] A.Y. Kitaev, „Periodic table for topological insulators and superconductors“, AIP Conference Proceedings **1134**, 22-30 (2009).

[7] S. Ryu, A.P. Schnyder, A. Furusaki, and A.W.W. Ludwig, „Topological insulators and superconductors: tenfold way and dimensional hierarchy“, New J. Phys. **12**, 065010 (2010).

[8] A.P. Schnyder and P.M.R. Brydon, „Topological surface states in nodal superconductors“, J. Phys.: Condens. Matter **27**, 243201 (2015).

[9] A.Yu. Kitaev, „Unpaired Majorana fermions in quantum wires“, Physics-Uspekhi **44**, 131 (2001).

[10] C. Nayak, S.H. Simon, A. Stern, M. Freedman, and S. Das Sarma, „Non-Abelian anyons and topological quantum computation“, Rev. Mod. Phys. **80**, 1083–1159 (2008).

[11] T.-P. Choy, J.M. Edge, A.R. Akhmerov, and C.W.J. Beenakker, „Majorana fermions emerging from magnetic nanoparticles on a superconductor without spin-orbit coupling“, Phys. Rev. B **84**, 195442 (2011).

[12] S. Nadj-Perge, I.K. Drozdov, B.A. Bernevig, and A. Yazdani, „Proposal for realizing Majorana fermions in chains of magnetic atoms on a superconductor“, Phys. Rev. B **88**, 020407 (2013).

[13] S. Nadj-Perge, I.K. Drozdov, J. Li, H. Chen, S. Jeon, J. Seo, A.H. MacDonald, B.A. Bernevig, and A. Yazdani, „Observation of Majorana fermions in ferromagnetic atomic chains on a superconductor“, Science **346**, 602–607 (2014).

[14] W. Chen and A.P. Schnyder, „Majorana edge states in superconductor-noncollinear magnet interfaces“, Phys. Rev. B **92**, 214502 (2015).

[15] P.M.R. Brydon, S. Das Sarma, H.-Y. Hui, and J.D. Sau, „Topological Yu-Shiba-Rusinov chain from spin-orbit coupling“, Phys. Rev. B **91**, 064505 (2015).

[16] L.K. Grover, „A Fast Quantum Mechanical Algorithm for Database Search“, In „Proceedings of the Twenty-eighth Annual ACM Symposium on Theory of Computing“ (ACM, New York, NY, USA, 1996).

[17] P.W. Shor, „Polynomial-Time Algorithms for Prime Factorization and Discrete Logarithms on a Quantum Computer“, SIAM Journal on Computing **26**, 1484-1509 (1997).

[18] R. Jördens, N. Strohmaier, K. Günter, H. Moritz, and T. Esslinger, „A Mott insulator of fermionic atoms in an optical lattice“, Nature **455**, 204–207 (2008).

[19] U. Schneider, L. Hackermüller, S. Will, Th. Best, I. Bloch, T.A. Costi, R.W. Helmes, D. Rasch, and A. Rosch, „Metallic and Insulating Phases of Repulsively Interacting Fermions in a 3D Optical Lattice“, Science **322**, 1520–1525 (2008).

[20] H.-P. Breuer and F. Petruccione, *The Theory of Open Quantum Systems* (Oxford University Press, 2002).

[21] N. Moiseyev, *Non-Hermitian Quantum Mechanics* (Cambridge University Press, 2011).

[22] M.-A. Nielsen and I.-L. Chuang, *Quantum Computation and Quantum Information: 10th Anniversary Edition* (Cambridge University Press, 2010).

[23] E. Knill, „Quantum computing with realistically noisy devices“, Nature **434**, 39–44 (2005).

[24] A.Yu. Kitaev, „Fault-tolerant quantum computation by anyons“, Annals of Physics **303**, 2–30 (2003).

[25] H. Weimer, M. Müller, I. Lesanovsky, P. Zoller, and H.P. Büchler, „A Rydberg quantum simulator“, Nature Physics **6**, 382–388 (2010).

[26] V. Mourik, K. Zuo, S.M. Frolov, S.R. Plissard, E.P.A.M. Bakkers, and L.P. Kouwenhoven, „Signatures of Majorana Fermions in Hybrid Superconductor-Semiconductor Nanowire Devices“, Science **336**, 1003–1007 (2012).

[27] J. Zak, „Berry's phase for energy bands in solids“, Phys. Rev. Lett. **62**, 2747–2750 (1989).

[28] J.C. Budich and E. Ardonne, „Equivalent topological invariants for one-dimensional Majorana wires in symmetry class D“, Phys. Rev. B **88**, 075419 (2013).

[29] S. Bravyi and R. König, „Disorder-Assisted Error Correction in Majorana Chains“, Communications in Mathematical Physics **316**, 641–692 (2012).

[30] S.R. Elliott and M. Franz, „*Colloquium:* Majorana fermions in nuclear, particle, and solid-state physics“, Rev. Mod. Phys. **87**, 137–163 (2015).

[31] B.A. Bernevig and T.L. Hughes, *Topological Insulators and Topological Superconductors*, 1 ed. (Princeton University Press, 2013).

[32] N. Read and D. Green, „Paired states of fermions in two dimensions with breaking of parity and time-reversal symmetries and the fractional quantum Hall effect“, Phys. Rev. B **61**, 10267–10297 (2000).

[33] M. Sato and Y. Ando, „Topological Superconductors“, arXiv:1608.03395 (2016).

[34] G.D. Mahan, *Many-Particle Physics* (Springer, 2000).

[35] S. Kashiwaya, H. Kashiwaya, H. Kambara, T. Furuta, H. Yaguchi, Y. Tanaka, and Y. Maeno, „Edge States of Sr_2RuO_4 Detected by In-Plane Tunneling Spectroscopy“, Phys. Rev. Lett. **107**, 077003 (2011).

[36] F. Pientka, L.I. Glazman, and F. von Oppen, „Topological superconducting phase in helical Shiba chains“, Phys. Rev. B **88**, 155420 (2013).

[37] B. Braunecker, G.I. Japaridze, J. Klinovaja, and D. Loss, „Spin-selective Peierls transition in interacting one-dimensional conductors with spin-orbit interaction“, Phys. Rev. B **82**, 045127 (2010).

[38] M. Sato, Y. Takahashi, and S. Fujimoto, „Non-Abelian topological orders and Majorana fermions in spin-singlet superconductors“, Phys. Rev. B **82**, 134521 (2010).

[39] A.V. Balatsky, I. Vekhter, and J.-X. Zhu, „Impurity-induced states in conventional and unconventional superconductors“, Rev. Mod. Phys. **78**, 373–433 (2006).

[40] L. Yu, „Bound state in superconductors with paramagnetic impurities“, Acta Physica Sinica **21**, 75 (1965).

[41] H. Shiba, „Classical spins in superconductors“, Prog. Theor. Phys. **40**, 435–451 (1968).

[42] A.I. Rusinov, „On the theory of gapless superconductivity in alloys containing paramagnetic impurities“, Soviet Physics JETP **29**, 1101–1106 (1969).

[43] S. Nakosai, Y. Tanaka, and N. Nagaosa, „Two-dimensional *p*-wave superconducting states with magnetic moments on a conventional *s*-wave superconductor“, Phys. Rev. B **88**, 180503 (2013).

[44] M.A. Ruderman and C. Kittel, „Indirect Exchange Coupling of Nuclear Magnetic Moments by Conduction Electrons“, Phys. Rev. **96**, 99–102 (1954).

[45] T. Kasuya, „A Theory of Metallic Ferro- and Antiferromagnetism on Zener's Model“, Prog. Theor. Phys. **16**, 45–57 (1956).

[46] K. Yosida, „Magnetic Properties of Cu-Mn Alloys“, Phys. Rev. **106**, 893–898 (1957).

[47] I. Dzyaloshinsky, „A thermodynamic theory of "weak" ferromagnetism of antiferromagnetics“, J. Phys. Chem. Solids **4**, 241–255 (1958).

[48] T. Moriya, „Anisotropic Superexchange Interaction and Weak Ferromagnetism“, Phys. Rev. **120**, 91–98 (1960).

[49] M. Schecter, K. Flensberg, M.H. Christensen, B.M. Andersen, and J. Paaske, „Self-organized topological superconductivity in a Yu-Shiba-Rusinov chain“, Phys. Rev. B **93**, 140503 (2016).

[50] M.H. Christensen, M. Schecter, K. Flensberg, B.M. Andersen, and J. Paaske, „Spiral magnetic order and topological superconductivity in a chain of magnetic adatoms on a two-dimensional superconductor“, arXiv:1607.08190 (2016).

[51] K.V. Samokhin, „Spin–orbit coupling and semiclassical electron dynamics in noncentrosymmetric metals“, Annals of Physics **324**, 2385-2407 (2009).

[52] J. Li, T. Neupert, Z.J. Wang, A.H. MacDonald, A. Yazdani, and B.A. Bernevig, „Two-dimensional chiral topological superconductivity in Shiba lattices“, Nat. Commun. **7**, 12297 (2016).

[53] M. Wimmer, „Algorithm 923: Efficient Numerical Computation of the Pfaffian for Dense and Banded Skew-Symmetric Matrices“, ACM Trans. Math. Softw. **38**, 30:1–30:17 (2012).

[54] T. Fukui, Y. Hatsugai, and H. Suzuki, „Chern Numbers in Discretized Brillouin Zone: Efficient Method of Computing (Spin) Hall Conductances“, J. Phys. Soc. Jpn. **74**, 1674-1677 (2005).

[55] Y.-F. Zhang, Y.-Y. Yang, Y. Ju, L. Sheng, R. Shen, D.-N. Sheng, and D.-Y. Xing, „Coupling-matrix approach to the Chern number calculation in disordered systems“, Chinese Physics B **22**, 117312 (2013).